The Astrophysical Journal, 572:636–662, 2002 June 10

ENERGY BALANCE IN THE SOLAR TRANSITION REGION. IV. HYDROGEN AND HELIUM MASS FLOWS WITH DIFFUSION

J. M. Fontenla,[1] E. H. Avrett,[2] and R. Loeser[2]
Received 2001 September 10; accepted 2002 February 12

ABSTRACT

In this paper we extend our previous modeling of energy balance in the chromosphere-corona transition region to cases with particle and mass flows. The cases considered here are quasi-steady and satisfy the momentum and energy balance equations in the transition region. We assume one-dimensional geometry and include the flow velocity terms in all equations, but we neglect the partial derivatives with respect to time. We present a complete and physically consistent formulation and method for solving the non-LTE and energy balance equations in these situations, including both particle diffusion and flows of H and He. Our calculations include partial frequency redistribution in the Lyα and Lyβ lines. Our results show quantitatively how mass flows affect the ionization and radiative losses of H and He, thereby affecting the structure and extent of the transition region. Furthermore, our computations show that the H and He line profiles are greatly affected by flows. We find that line shifts are much less important than the changes in line intensity and central reversal as a result of the influence of flows on the excitation and ionization. In this paper we use fixed conditions at the base of the transition region and in the underlying chromosphere. Our intent is to show the physical effects of flows on the transition region, not to match any particular observations. However, our computed Lyα profiles can account for the range of observed high spectral and spatial resolution from the quiet Sun. We suggest that dedicated modeling of specific sequences of observations based on physically consistent methods like those presented here will substantially improve our understanding of the energy balance in the chromosphere and corona.

Subject headings: diffusion — hydrodynamics — line: formation — radiative transfer — Sun: transition region

1. INTRODUCTION

In our previous papers, Fontenla, Avrett, & Loeser (1990, 1991, 1993, hereafter FAL90, FAL91, FAL93), we developed quasi-static models of the solar atmosphere, using separate one-dimensional models to represent different quiet and active solar features (see the FAL papers for the physical justification of these approximations in the modeling of the transition region). These models, as well as earlier ones (e.g., Vernazza, Avrett, & Loeser 1981, hereafter VAL81), included a turbulent velocity (often called "microturbulent velocity" in the literature) both to broaden spectral lines and to modify the equation of hydrostatic equilibrium by adding a Bernoulli term that represents a dynamic pressure contribution (see the "turbulent pressure velocity" in the VAL81 and FAL papers). The modified equation was used to determine the density stratification in the atmosphere that, because of this added term, departs from a hydrostatic stratification that balances only gas pressure and gravity. We introduced the important effects of hydrogen and helium diffusion in the chromosphere-corona transition region and for the first time obtained reasonable agreement between calculated and observed line profiles for hydrogen and helium, including general agreement with the well-observed hydrogen Lyα line profile (Fontenla, Reichmann, & Tandberg-Hanssen 1988, hereafter FRT88). We showed that energy flow by thermal conduction alone, without diffusion, cannot account for the observed Lyα line profile but that including diffusion solves this problem. In the present paper we extend the model calculations to include particle and mass flows in addition to diffusion.

Many papers have studied quasi-steady flows in the transition region, e.g., Boris & Mariska (1982), Craig & McClymont (1986), McClymont & Craig (1987), Mariska (1988), and McClymont (1989). It is not possible for us to address all of them; for a review, see Mariska (1992). Here we just mention that these papers deal in detail with the upper transition region and coronal loops where H and He are fully ionized, and these papers use the radiative losses determined by Cox & Tucker (1969) for optically thin plasmas. These papers are not applicable to the lower transition region and chromosphere where H and He are only partially ionized and where the resonance lines of H and He must be computed from detailed solutions of the radiative transfer equations. In addition, these papers do not include the complicated processes of particle diffusion and radiative transfer addressed in the FAL papers. Nevertheless, they indicated that the observed redshifts in transition region lines might be explained by quasi-steady flows in coronal loops.

More recent calculations have been carried out, e.g., by Hansteen & Leer (1995), including velocities in models that also assume a fully ionized plasma. Again, while this assumption is valid in the corona and in the upper transition region (depending on the velocity), it is inadequate for the low transition region where H and He are only partially ionized.

Woods & Holzer (1991) consider a multicomponent plasma composed of electrons, protons, ionized helium, and minor ion species. These calculations use the Saint-Maurice & Schunk (1977a, 1977b) treatment of particle diffusion and heat flow (which is based on a different method but in most

[1] 1874 MacCullen Drive, Erie, CO 80516; jfonten750@earthlink.net.
[2] Smithsonian Astrophysical Observatory, Harvard-Smithsonian Center for Astrophysics, 60 Garden Street, Cambridge, MA 02138; eavrett@cfa.harvard.edu, rloeser@cfa.harvard.edu.

respects is equivalent to that used in the FAL papers). Woods & Holzer (1991) make the point that earlier model estimates of minor ion line intensities may not be accurate because the effects of flow and particle diffusion on these ion abundances and ionization degrees were not included.

Hansteen, Leer, & Holzer (1997) carried out calculations that also include ionization, energy flow, and particle diffusion, following again the Saint-Maurice & Schunk (1977a, 1977b) formulation. They consider partial H and He ionization, variable helium abundance, and possible differences between the electron, H, and He temperatures, and they explore various possible parameters related to the solar wind. They do not include the detailed effects of radiative transfer, H and He excitation, ionization, and radiative losses in a manner consistent with particle diffusion and flows. Instead, for simplicity, they make assumptions such as (1) taking photoionization rates from VAL81 that were determined for certain empirical static models without diffusion or energy balance; and (2) taking H, He, and other radiative losses from Rosner, Tucker, & Vaiana (1978; based on numerical expressions from the Cox & Tucker 1969 calculations) that assume local collisional ionization; these radiative losses do not include particle flows or diffusion and are not consistent with their models. As we showed in the FAL calculations, these approximations differ very substantially from the values that result from fully consistent solutions of the radiative transfer and statistical equilibrium equations with particle diffusion. Moreover, as we show here, particle flows also have important effects on the H and He line intensities, radiative losses, and ionization rates (and consequently on the ionization energy flux). Hansteen et al. (1997) recognize that their optically thin losses are not valid in the chromosphere (our detailed computations indicate that they are not valid in the lower transition region either), and they compute these radiative losses in an ad hoc manner that does not include the correct dependence of the radiative losses on the temperature and density structure of the atmosphere. Despite these shortcomings, many important conclusions result from their paper, although it is sometimes unclear how some of them may be affected by the ad hoc assumptions made.

Chae, Yun, & Poland (1997, hereafter CYP97) studied the effects of flow velocities and for the first time introduced the solution of the statistical equilibrium and radiative transfer equations in an energy balance model including flows. However, they assumed level populations, ionization, and radiative losses that are derived from a static model calculation and that may not be fully consistent with the velocities and the temperature stratifications they compute. In § 6 we comment further on how this paper improves on the CYP97 results.

In this paper we carry out consistent calculations of level populations and ionization at all heights, as well as a consistent calculation of energy balance in the lower transition region including the effects of diffusion and mass flows at heights where H and He change from being mostly neutral to almost fully ionized and where the important optically thick resonance lines of H and He are formed. For completeness we also include energy balance calculations in the upper transition region where H and He are almost fully ionized, but here the results depend on approximate formulae for the radiative losses due to other constituents.

Our previous calculations (FAL90; FAL91; FAL93) solved the H and He radiative transfer and statistical equilibrium equations including particle diffusion but assumed zero net H and He particle fluxes and consequently zero mass flow. In the transition region (except where strong inflows occur; see § 5) diffusion is very important because the temperature gradient, and thus the corresponding ionization gradient, is very large. Diffusion causes a reduction of the ionization gradient, as a result of H atoms diffusing outward and protons diffusing inward. Helium diffusion is more complicated and shows outward He I and inward He III diffusion, while He II diffusion varies with height. In addition, helium diffusion is strongly affected by the diffusion of hydrogen atoms and protons. In FAL91 and FAL93 we presented the fully consistent formulation for static energy balance cases, some numerical solutions for typical portions of the solar atmosphere, and also some approximate formulae that summarize these computations and that can be used to estimate radiative losses and effective heat transport coefficients.

In this paper we describe a computational method that includes particle flows and explore the effects of mass flows (in which particle flow velocities are the same for H and He). We consider the combined effects of diffusion and particle flows on the ionization and excitation of hydrogen and helium and on the momentum and energy balance. We have incorporated these physical processes into the PANDORA computer program. Earlier versions of this program were used in the FAL papers and in previous ones discussed by Avrett & Loeser (1992). We again assume one-dimensional geometry, with height as the only measure of position (see our discussion in FAL93). We carry out our computations as in the FAL papers, but now we introduce prescribed mass- and particle-conserving hydrogen and helium flows. Thus, we compute results for two parameters, the flux $F_{\rm H}$ of hydrogen particles (H atoms and protons) and the flux $F_{\rm He}$ of helium particles (He I, He II, and He III). We assume that these fluxes are constant through the transition region because if an initial change in a boundary condition occurs, the resulting dynamics would rapidly lead to a flux that is constant with height in a timescale comparable with the sound travel time across the region. Since the lower transition region (where 10^4 K $< T < 10^5$ K) is very thin (except for strong inflows, as we show in § 5), this travel time is a few seconds. Consequently, the constant flux approximation is valid for cases in which the velocity at the boundary varies on timescales of many seconds or longer (see FAL93). In our calculation a time-dependent approach has no advantage since we are not dealing with pulsed or explosive phenomena (such as shock waves or the impulsive phase of solar flares) but rather with quiet and moderately active regions of the solar atmosphere that are observed to undergo moderate changes in timescales of minutes. As in our previous calculations, we prescribe the temperature structure of the underlying chromosphere and photosphere. As the density rapidly increases with decreasing height in the upper chromosphere, the flow velocities quickly become very small but still have some effects in the upper chromosphere. These effects are fully included in our calculations since we include the velocity terms throughout the chromosphere. The effects are negligible in the temperature minimum region and the photosphere. In this paper we present the method we use for these calculations and some of the results we obtained.

In our previous quasi-static models we determined the temperature versus height structure of the transition region

by solving the energy balance equation. In these models the radiative losses are balanced by the inward flux of heat (including ionization energy) from the corona. Part of the heat flux is due to thermal conduction, mainly by electrons (although H atom conduction contributes at low ionization and low temperature). However, a large contribution to this inward energy flow is due to the ionization energy that the protons carry as they diffuse into the lower transition region. Protons recombine at low temperatures and thus release their ionization energy. Including such diffusion and inward energy flow leads to a smaller temperature gradient and a more extended transition region than would result from thermal conduction alone (see FAL90, § 6). In this paper we define the total heat flux as the total of the flux of thermal, ionization, and excitation energy, as well as the particle enthalpy flux.

Since we solve in detail only H and He, our models of the temperature variation with height apply mainly to the low transition region, from the chromosphere to about 10^5 K (depending on the hydrogen and helium flows) because at these temperatures H and He are the main contributors to the radiative losses and energy transport (in addition to electron thermal conduction and enthalpy flow). At higher temperatures other species dominate as H and He become completely ionized. More work is needed to carry out consistent calculations for species other than H and He, including both diffusion and flow velocity (J. M. Fontenla & M. Rovira 2002, in preparation). For the present we have approximated the effects of these other species in the same way as in our previous papers by using the Cox & Tucker (1969) radiative losses, so that we can extend our calculations out to coronal temperatures.

In this paper we present a set of results showing the complete effects of velocities for models each having a temperature distribution $T(z)$ in the transition region individually determined by energy balance. We compare the results with various mass flows to a static model having a temperature distribution also determined by energy balance. This static model temperature distribution is similar to that of the static model C used by Fontenla et al. (1999), but slightly modified at the base of the transition region, which leads to some changes throughout the transition region. Furthermore, this static model is extended to higher temperatures in the low corona.

We show the equations and methods used to solve the statistical equilibrium and radiative transfer equations including both diffusion and velocity terms. Next, we show the momentum balance equations we solve in order to determine the gas pressure and density throughout the model. Then we describe the method we use to determine the temperature versus height in these models by solving the energy balance equation that includes heat conduction, enthalpy, and ionization energy flux terms. The radiative losses are computed from the detailed calculations described above, and all computations are iterated until all the quantities are consistent with the radiative transfer and statistical equilibrium equations as well as with the energy balance and momentum balance equations. The temperature structure of the underlying chromosphere and photosphere must still be prescribed as indicated above since we cannot compute the chromospheric temperature structure in energy balance. That is because the mechanism of chromospheric heating is still unknown and because such a full energy balance computation requires knowledge of the dependence of the heating on physical parameters such as height, density, electron density, temperature, and magnetic field. It is not realistic to specify a fixed incident radiation on the transition region from the underlying chromosphere because radiation from the transition region affects the excitation and ionization conditions in the chromosphere, thereby affecting the outward chromospheric radiation. (The radiation from the transition region also affects the pressure at the top of the chromosphere to a small extent.) To solve the problem in a consistent way, we include the self-consistent calculation of the underlying chromosphere and photosphere in such a way that all the complex interactions are solved at once.

The purpose of these calculations is to show how mass flows affect the equilibrium temperature distribution in the transition region and the H and He lines. We show the various temperature distributions, ionization fractions, radiative losses, and energy flux variations with height and provide an interpretation of the results. Finally, we present the H and He line profiles for the resulting inflow and outflow models and infer some characteristics that are useful to interpret observations. The line profiles shown here are intended to illustrate the general effects of inflows and outflows, but we give results for only one underlying chromospheric model, that corresponding to the average quiet Sun. In addition, we neglect the mechanical heating in the transition region (other than that due to the steady flows). In a subsequent paper we will include results for the other chromospheric structures and for mechanical heating in the transition region. This subsequent paper will be more suitable for detailed comparison with observations.

2. IONIZATION EQUILIBRIUM EQUATIONS

Here we briefly review the basic theory for the various types of velocities, show how these velocities are defined, and show how they cause the ionization balance to differ from the local static ionization balance. Corresponding departures from local static equilibrium can be expected in the level populations as well, but in the cases we consider these are less important than the ionization effects because of the large transition rates between the levels of the atoms we study (a possible exception is the lowest triplet energy level of the He atom).

The ionization equilibrium for ionization stage i of a given element k is described by the equation

$$\frac{\partial n_{ik}}{\partial t} + \nabla \cdot (n_{ik} \boldsymbol{V}_{ik}) = R_{ik} \ , \tag{1}$$

where n_{ik} is the total number density of all energy levels in this ionization stage, R_{ik} is the net creation rate for ions in stage i, and $\boldsymbol{V}_{ik}$ is the mean velocity of those ions.

Using $i + 1$ and $i - 1$ to refer to the next ionization stages higher and lower than i, we can write

$$R_{ik} = n_{i+1,k} P_{i+1,i,k} + n_{i-1,k} P_{i-1,i,k} - n_{ik}(P_{i,i+1,k} + P_{i,i-1,k}) \ , \tag{2}$$

where $P_{i,j,k}$ is the transition rate to the final ionization stage j per particle of the element k in the initial ionization stage i.

The velocity $\boldsymbol{V}_{ik}$ can be decomposed into three components: (1) the center-of-mass velocity $\boldsymbol{U}$ given by the motion of all types of particles weighted by their mass and number

density,

$$\boldsymbol{U} = \frac{\sum_{i,k} m_k n_{ik} \boldsymbol{V}_{ik}}{\sum_{i,k} m_k n_{ik}} , \tag{3}$$

(2) the velocity $\boldsymbol{v}_k$ of each element relative to the center-of-mass velocity,

$$\boldsymbol{v}_k = \frac{\sum_i n_{ik} \boldsymbol{V}_{ik}}{\sum_i n_{ik}} - \boldsymbol{U} , \tag{4}$$

and (3) the diffusion velocity $\boldsymbol{v}_{ik}$ of each ionization stage relative to $(\boldsymbol{v}_k + \boldsymbol{U})$,

$$\boldsymbol{v}_{ik} = \boldsymbol{V}_{ik} - (\boldsymbol{v}_k + \boldsymbol{U}) . \tag{5}$$

With these definitions, equation (1) may be written as

$$\frac{\partial n_{ik}}{\partial t} + \nabla \cdot [n_{ik}(\boldsymbol{v}_{ik} + \boldsymbol{v}_k + \boldsymbol{U})] = R_{ik} , \tag{6}$$

showing how the three velocities are involved in determining n_{ik}. The decomposition is useful because, as we explain below, these three components of the velocity result from different physical phenomena, and different particle and momentum conservation constraints apply to each component.

The lower transition region between the solar chromosphere and corona is a very thin layer (at least in the static case) that occurs at various heights and orientations above the photosphere. For our purposes this layer can be locally approximated by a one-dimensional stratification as we explain in the previous FAL papers. Thus, in equation (6) we neglect horizontal variations and consider spatial variations only as functions of the height coordinate z.

Furthermore, the steady state approximation is reasonable in the transition region because ions are quickly transported, in a few seconds, by flows and diffusion to the locations where they ionize or recombine. Since our modeling does not apply to impulsive heating cases, we drop the partial time derivative term and write equation (6) as

$$\frac{d}{dz}[n_{ik}(v_{ik} + v_k + U)] = R_{ik} , \tag{7}$$

where $n_{ik}(v_{ik} + v_k + U)$ is the ionization stage flow.

The mass velocity U is not affected by atomic collisions but only by macroscopic forces, and the conservation of mass gives

$$\frac{d}{dz}(\rho U) = 0 , \tag{8}$$

where ρ is the mass density. The integration of this equation defines the constant mass flow, $F_m = \rho U$.

The velocity v_k of a given element relative to U is determined by the abundance gradient and by various forces acting on the given element, moderated by elastic and inelastic collisions between different elements and with free electrons. In the relatively high densities of the solar atmosphere out to the lower corona these velocities are expected to be in the diffusion regime where collisions drive the particle distributions close to a Maxwellian function centered around the velocity U. Since we do not consider nuclear reactions, the total number density

$$n_k = \sum_i n_{ik} \tag{9}$$

of element k satisfies the element conservation equation

$$\frac{d}{dz}[n_k(v_k + U)] = 0 . \tag{10}$$

The integration of this equation defines the constant element flow,

$$F_k = n_k(v_k + U) . \tag{11}$$

The remaining diffusion velocity v_{ik} is driven by various forces (including electric fields and ionization gradients) and is slowed by collisions. Radiative and collisional interactions transform ions from one stage to another, and in the transition region this induces strong ionization gradients that lead to significant ion diffusion velocities v_{ik}. Thus, the ionization stage flow in equation (7) is not constant with height.

Using the element flow F_k, we can write equation (7) as

$$\frac{d}{dz}\left[n_{ik}\left(v_{ik} + \frac{F_k}{n_k}\right)\right] = R_{ik} . \tag{12}$$

Defining the ionization fraction $y_{ik} = n_{ik}/n_k$, we can write

$$\frac{d}{dz}[y_{ik}(n_k v_{ik} + F_k)] + r_{ik} y_{ik} = s_{ik} , \tag{13}$$

where, from equation (2),

$$\begin{aligned} r_{ik} &= n_k(P_{i,i+1,k} + P_{i,i-1,k}) , \\ s_{ik} &= n_{i+1,k} P_{i+1,i,k} + n_{i-1,k} P_{i-1,i,k} . \end{aligned} \tag{14}$$

The system given by equation (13) for all stages of ionization of a given element is redundant, since the sum of all such equations is zero. Thus, we consider these equations for all but the fully ionized stage and supplement them with equation (9). In the next sections we use equation (9) to modify the above expressions for r_{ik} and s_{ik} in order to obtain a set of equations that is better conditioned than if equation (9) were used separately.

The basic equations for the H and He diffusion velocities v_{ik} appear in FAL93, and here we restate some of them in summary form only. In general, the diffusion velocities can be expressed as linear functions of the logarithmic gradients of the " thermodynamic forces " (FAL90; FAL91; FAL93). This expression is

$$v_{ik} = \sum_n D_{ikn} Z_n , \tag{15}$$

where D_{ikn} is the diffusion coefficient that expresses the dependence of the diffusion velocity of element k in ionization stage i on the thermodynamic force Z_n. In this paper we use the same expressions for Z_n that we gave in FAL93 (see eqs. [15] and [16] in that paper).

As we did in our previous papers, we express the relative diffusion velocities $u_{i,i+1,k}$ between consecutive ionization stages i and $i+1$ of element k as linear functions of the thermodynamic forces and then express the diffusion velocities v_{ik} as linear functions of these relative diffusion velocities.

The definitions of the relative diffusion velocities as well as the expressions of the diffusion velocities in terms of the relative diffusion velocities are shown in FAL93 (see eqs. [14] and [17] in that paper). Although we solve the ionization equations in a slightly different way here, FAL93 gives the remaining details on the treatment of diffusion.

In this paper, as in the FAL papers, we neglect gravitational thermodynamic forces. From particle transport theory, the gravitational thermodynamic force would be $Z_g = H^{-1}$, where H is the gravitational scale height. The significant effect of this thermodynamic force would be to drive the gravitational settling of heavier elements in lower atmospheric layers. Details on the problem of element separation and diffusion effects can be found in Fontenla & Avrett (1992). In the present paper we assume that in the transition region these effects are not very important because if gravitational settling has not yet reached equilibrium (e.g., when we assume constant He abundance), there would be only a very small difference in the elemental diffusion velocities of H and He (i.e., $v_{\rm H} \neq v_{\rm He}$) that would drive He downward and H upward. In addition, after the He abundance distribution has reached equilibrium within the transition region, this abundance variation would not be very significant for a transition region thickness that is much smaller than the height scale. However, these assumptions need further study. In any case, the gravitational settling processes are very complicated. They may involve long timescales and thus are very much affected by time-dependent effects that may mix the material. They also depend on the boundary conditions at the underlying chromospheric layers and in the overlying coronal layers. All the equations in this paper allow for a difference between H and He elemental diffusion velocities and for a variable He abundance, but in the numerical cases we compute we assume $v_{\rm H} = v_{\rm He} = 0$ and constant He abundance for simplicity. Indeed, the gravitational settling effects could be very significant in the chromosphere, and in later papers we will study these effects in more detail.

2.1. *Hydrogen Flow and Diffusion*

In the case of hydrogen we consider the proton number density n_p (the H II density); the atomic hydrogen number density $n_a = \sum_\ell n_\ell$ (the H I density), where the sum is over all bound levels ℓ; and the total hydrogen density $n_{\rm H} = n_a + n_p$. Equation (2) for the net creation rate of neutral hydrogen atoms can be written as

$$R_a = n_p \sum_\ell P_{\kappa\ell} - \sum_\ell n_\ell P_{\ell\kappa} = (n_{\rm H} - n_a) \sum_\ell P_{\kappa\ell} - n_a \sum_\ell \left(\frac{n_\ell}{n_a}\right) P_{\ell\kappa} \ , \tag{16}$$

where the index κ designates the continuum (the ionized H or proton state) and $P_{\kappa\ell}$ and $P_{\ell\kappa}$ are the recombination and ionization rates to and from level ℓ. The second form of the right-hand side of the equation illustrates how we handle the redundancy of equation (7) for neutral and ionized hydrogen. We use only the equation for neutral hydrogen and eliminate the number density of ionized hydrogen using equation (9), which is the expression for $n_{\rm H}$.

For hydrogen, equation (13) applies with $y_a = n_a/n_{\rm H}$ the atomic hydrogen fraction and $F_k = F_{\rm H}$ the total hydrogen particle flow, but we replace the definitions of equation (14) by

$$r = n_{\rm H} \sum_\ell \left[P_{\kappa\ell} + \left(\frac{n_\ell}{n_a}\right) P_{\ell\kappa} \right] \ ,$$
$$s = n_{\rm H} \sum_\ell P_{\kappa\ell} \ . \tag{17}$$

The ionization equilibrium equation (13) for H is

$$\frac{d}{dz}\left[y_a(n_{\rm H} v_a + F_{\rm H})\right] + r y_a = s \ , \tag{18}$$

where v_a is the diffusion velocity v_{ik} for hydrogen atoms. Using the derivations in FAL93 (mainly eqs. [16] and [17] in that paper), we can write

$$v_a = \frac{x}{1+x}\left(d_{11}\frac{d\ln x}{dz} + \Delta_1\right) \ , \tag{19}$$

where $x = n_p/n_a$ and

$$\Delta_1 = d_{12}Z_a + d_{13}Z_b + d_{14}Z_c + d_{15}Z_T \ . \tag{20}$$

It can be shown without difficulty that

$$n_a \frac{x}{1+x}\frac{d\ln x}{dz} = -n_{\rm H}\frac{dy_a}{dz} \ , \tag{21}$$

where $y_a = n_a/n_{\rm H}$ as before. Thus, equation (18) becomes

$$\frac{d}{dz}\left(g y_a - f\frac{dy_a}{dz}\right) + r y_a = s \ , \tag{22}$$

where

$$f = d_{11} n_{\rm H} \ ,$$
$$g = F_{\rm H} + n_p \Delta_1 \ , \tag{23}$$

and where r and s are given by equation (17). Appendix A gives the numerical method we use for solving the differential equation (22).

As a result of radiative transfer, the quantities r and s depend not only on the local values of the ionization and recombination rates but also on the level populations and ionization rates at other heights. We start the calculations with values of n_ℓ/n_a from previous calculations. Then, after every calculation of n_a by the method described above, each level number density is corrected by first normalizing it to the new n_a and then computing the solution of the statistical equilibrium and radiative transfer equations for all levels, as is explained below. This procedure is iterated until convergence to the proper solution is achieved.

The net rate into bound level m from the ionized stage and from all other bound levels is given by

$$R_m = \sum_{\ell\neq m} n_\ell P_{\ell m} + n_\kappa P_{\kappa m} - n_m\left(\sum_{\ell\neq m} P_{m\ell} + P_{m\kappa}\right) \ , \tag{24}$$

and R_a in equation (16) is the sum of R_m, over all m (since the bound-bound transition terms cancel in this sum). An equation similar to equation (12) can be written for each bound level m,

$$\frac{d}{dz}\left[n_m\left(v_a + \frac{F_{\rm H}}{n_{\rm H}}\right)\right] = R_m \ . \tag{25}$$

Because of the large transition rates between bound levels,

we assume that all the bound levels have the same diffusion velocity v_a. Thus, to solve for the hydrogen level populations, we use the statistical equilibrium equation

$$n_m\left(\sum_{\ell\neq m} P_{m\ell} + P_{m\kappa} + G_m\right) = \sum_{\ell\neq m} n_\ell P_{\ell m} + n_p P_{\kappa m} \ , \quad (26)$$

where

$$G_m = \frac{1}{n_m}\frac{d}{dz}\left[n_m\left(v_a + \frac{F_{\rm H}}{n_{\rm H}}\right)\right] \ . \quad (27)$$

We use the new y_a obtained from a solution of equation (22) along with the previous ratios n_m/n_a to obtain $n_m/n_{\rm H}$ and thus G_m. Then we solve the set of statistical equilibrium equations given by equation (26) for all levels, coupled with the radiative transfer equations, to obtain new values of n_m and n_p with the constraint that they add up to the given $n_{\rm H}$. Note that this solution involves excitation, de-excitation, ionization, and recombination rates that depend on radiation intensities, which in turn depend on the number densities throughout the atmosphere according to the equations of radiative transfer. The same applies to the photoionization rates that occur in the expression for r. Thus, the statistical equilibrium equations given by equation (26) are solved together with the transfer equations for all these radiative transitions. Such solutions have been discussed extensively in the literature (e.g., Vernazza, Avrett, & Loeser 1973; Mihalas 1978; Avrett & Loeser 1992) and are not reviewed here.

Adding the G_m term to each ionization rate $P_{\ell m}$ in equation (26) incorporates the effect of flows and diffusion into the statistical equilibrium equations for the number densities n_m, but G_m has a complex dependence on the number densities. We have developed the iterative methods of solution described here to solve for these interdependent quantities. As in our previous papers, we solve the radiative transfer and statistical equilibrium equations for C, Si, Al, Mg, Ca, Fe, Na, and other constituents, in addition to H and He, to determine the electron density and the various opacities needed in the radiative transfer calculations. However, our solutions do not include particle diffusion or flows for these trace species.

2.2. *Helium Flow and Diffusion*

The ionization balance equations for helium are expressed by two independent equations of the form of equation (7) or (13) for He I and He II particle densities, n_α and n_β, respectively. A third equation for fully ionized He (viz., He III with particle density n_γ) would be redundant. As we did in the case of hydrogen, we complement the two equations for n_α and n_β with equation (9) for the helium total density, $n_{\rm He} = n_\alpha + n_\beta + n_\gamma$, and use the following expressions for the net rates of creation of He I and He II:

$$\begin{aligned} R_\alpha &= n_\beta P_{\beta\alpha} - n_\alpha P_{\alpha\beta} \\ &= (n_{\rm He} - n_\gamma - n_\alpha)P_{\beta\alpha} - n_\alpha P_{\alpha\beta} \ , \\ R_\beta &= n_\alpha P_{\alpha\beta} + n_\gamma P_{\gamma\beta} - n_\beta(P_{\beta\alpha} + P_{\beta\gamma}) \\ &= n_\alpha P_{\alpha\beta} + (n_{\rm He} - n_\beta - n_\alpha)P_{\gamma\beta} - n_\beta(P_{\beta\alpha} + P_{\beta\gamma}) \ . \end{aligned} \quad (28)$$

Thus, for helium, equation (13) applies for $y_\alpha = n_\alpha/n_{\rm He}$ and $y_\beta = n_\beta/n_{\rm He}$, the He I and He II fractions, and with definitions for r and s given by

$$\begin{aligned} r_\alpha &= n_{\rm He}(P_{\alpha\beta} + P_{\beta\alpha}) \ , \\ s_\alpha &= n_{\rm He}(1 - y_\gamma)P_{\beta\alpha} \ , \\ r_\beta &= n_{\rm He}(P_{\beta\gamma} + P_{\gamma\beta} + P_{\beta\alpha}) \ , \\ s_\beta &= n_{\rm He}[(1 - y_\alpha)P_{\gamma\beta} + y_\alpha P_{\alpha\beta}] \ , \end{aligned} \quad (29)$$

where $y_\gamma = n_\gamma/n_{\rm He} = 1 - y_\alpha - y_\beta$. The ionization equilibrium equations for He I and He II are

$$\begin{aligned} \frac{d}{dz}[y_\alpha(n_{\rm He}v_\alpha + F_{\rm He})] + r_\alpha y_\alpha &= s_\alpha \ , \\ \frac{d}{dz}[y_\beta(n_{\rm He}v_\beta + F_{\rm He})] + r_\beta y_\beta &= s_\beta \ . \end{aligned} \quad (30)$$

Using the expressions for the diffusion velocities of neutral and ionized He, v_α and v_β, derived in FAL93, these diffusion velocities are written as linear functions of the thermodynamic forces and lead to the following equations:

$$\begin{aligned} \frac{d}{dz}\left(g_\alpha y_\alpha - f_\alpha \frac{d}{dz}y_\alpha\right) + r_\alpha y_\alpha &= s_\alpha \ , \\ \frac{d}{dz}\left(g_\beta y_\beta - f_\beta \frac{d}{dz}y_\beta\right) + r_\beta y_\beta &= s_\beta \ , \end{aligned} \quad (31)$$

where, as shown in Appendix B,

$$\begin{aligned} f_\alpha &= n_{\rm He}\left\{\left(1 + \frac{y_\gamma}{y_\beta}\right)[d_{33}(1 - y_\gamma) - d_{34}y_\alpha] \right. \\ &\qquad \left. + \frac{y_\gamma}{y_\beta}[d_{43}(1 - y_\gamma) - d_{44}y_\alpha]\right\} \ , \\ g_\alpha &= F_{\rm He} + n_{\rm He}[(y_\beta + y_\gamma)\Delta_4 + y_\gamma\Delta_5] \ , \\ f_\beta &= n_{\rm He}\left\{d_{33}(1 - y_\gamma) - d_{34}y_\alpha \right. \\ &\qquad \left. - \frac{y_\gamma}{y_\alpha}[d_{43}(1 - y_\gamma) - d_{44}y_\alpha]\right\} \ , \\ g_\beta &= F_{\rm He} + n_{\rm He}\left(y_\gamma\Delta_7 - y_\alpha\Delta_6\right) \ . \end{aligned} \quad (32)$$

We again solve these equations using the numerical method described in Appendix A. Since the coefficients f and g depend on y_α, y_β, and y_γ, we iterate between the solutions of equation (31) for y_α and y_β until convergence is achieved. For He I, the number densities n_α and n_β are used in an equation similar to the hydrogen equation (27) to determine the coefficients G_m for the He I level m. Then the statistical equilibrium equations, similar to equation (26), are combined with the radiative transfer equations and solved to get new values of each n_m for He I.

The treatment of He II differs from that of H and He I since R_β in equation (28) includes the rates of ionization from and recombination to a lower ionization stage. Thus, for the ground level of He II we add the ionization equilibrium equation (12) for He I in order to eliminate these additional rates of recombination to and ionization from the lower ionization stage. We obtain

$$G_1({\rm He\ II}) = \frac{1}{n_1}\frac{d}{dz}\left[n_1\left(v_\beta + \frac{F_{\rm He}}{n_{\rm He}}\right) + n_\alpha\left(v_\alpha + \frac{F_{\rm He}}{n_{\rm He}}\right)\right] \quad (33)$$

for the ground level of He II, leaving the expression corresponding to equation (27) unchanged for He II levels $m > 1$.

Here we assume that there are no significant transitions between He I and the excited levels of He II. With G_m defined in this way, the statistical equilibrium equation (26) applies in all cases.

3. MOMENTUM BALANCE

In the cases in which flows are present we also need to consider how they affect the momentum balance equation from which we compute the gas pressure and consequently the H and He particle densities. For this we use the Navier-Stokes equation, neglecting viscosity and magnetic forces,

$$\frac{\partial U}{\partial t} + (\boldsymbol{U} \cdot \boldsymbol{\nabla}) U = g - \frac{\nabla p}{\rho} , \tag{34}$$

which in the present case reduces to

$$U \frac{dU}{dz} = g - \frac{1}{\rho} \frac{dp}{dz} , \tag{35}$$

where g is the gravitational acceleration and p is the gas pressure.

Since in the current models p is neither constant nor an analytic function of ρ, this equation has to be integrated numerically to yield the proper pressure and density as functions of height. We use the definition of F_m from the mass conservation equation (8) and write

$$F_m \frac{d}{dz}\left(\frac{F_m}{\rho}\right) + \frac{d}{dz}\left(\rho \frac{V_{\rm tp}^2}{2}\right) = \rho g - \frac{dp}{dz} , \tag{36}$$

where we include a Bernoulli term, the "turbulent pressure" gradient, based on the "turbulent pressure velocity" $V_{\rm tp}$. As discussed in the FAL papers, $V_{\rm tp}$ is inferred from the observed nonthermal widths of lines formed at various heights. The Doppler widths calculated for lines of heavy elements would be too small compared with observations without the addition of the so-called microturbulent velocity (e.g., Jefferies 1968). Using the microturbulent velocity values for a turbulent pressure velocity term added to the equation of hydrostatic equilibrium increases the vertical extent of the chromosphere and brings the semiempirical chromospheric models into better agreement with the limb observations of the He I 1083 nm line (see Avrett, Fontenla, & Loeser 1994). However, the detailed physical nature of the microturbulent velocity and the turbulent pressure is still not known. As their names indicate, they are assumed to be due to random dynamic effects, but it is not known to which spatial and temporal scales they correspond. Moreover, the large increase in the turbulent velocities observed in the transition region and coronal layers may correspond to a physical explanation very different from that for the photospheric lines. The turbulent velocities inferred from the optically thick photospheric lines are probably just unresolved random velocity distributions within the spatial resolution and may be confined to a narrow depth extent with minor vertical variations. However, in the optically thin lines from the transition region and corona the observed turbulent velocities may correspond mostly to different velocities of various structures along the line of sight because of the small opacity and very large spatial extent along the line of sight that may contribute to the observed profiles. In the chromospheric layers an intermediate situation may occur. In all cases, of course, lack of temporal resolution would also produce a widening of the lines as oscillations and dynamics would be temporally averaged. In this paper we do not elaborate on these complicated and physically unresolved issues and just use the turbulent velocities in the same way as they have been used in past work.

Collecting terms in equation (36) and considering that F_m is constant gives the following expression that we integrate numerically:

$$\frac{d}{dz}\left(\frac{F_m^2}{\rho} + \rho \frac{V_{\rm tp}^2}{2} + p\right) = \rho g . \tag{37}$$

The sum of terms in parentheses is the "total pressure" $p_{\rm total}$ that varies monotonically with z, even though p has slightly larger values in the lower transition region than at the top of the chromosphere (see § 5). The integration of equation (37) is done carefully to assure that the nearly exponential behavior is properly obtained depending on the mass flow and temperature variation with height. The first term inside the gradient on the left-hand side is often called "ram pressure" and takes into account the effects of the mass flow velocity on the density stratification of the atmosphere. Because of the ram pressure term, the static density stratification is not intermediate between the density stratifications of the inflow and outflow cases.

A problem with models including mass flow is that when the velocity reaches the sound speed (and viscosity is neglected) the combination of this equation with the energy balance equation leads to undefined mathematical conditions and erroneous numerical results. In this paper we avoid this difficulty by confining our models to the subsonic regions.

4. ENERGY BALANCE

We now address the computation of the temperature distribution for self-consistent energy balance models of the transition region. Our methods are similar to those in our earlier papers, but here we add the terms corresponding to the ionization energy and enthalpy transport due to the particle flows, $F_{\rm H}$ and $F_{\rm He}$, in addition to the corresponding terms due to the heat conduction and diffusion velocities already considered in our earlier papers.

As explained in § 9 of VAL81, we use the PANDORA computer program to compute the radiative losses due to H and He from the solutions of the equations shown above. These radiative losses now include the effects of flow as well as those of diffusion included in FAL93. To these radiative losses we add the free-free and other elemental radiative losses, using estimates based on the work of Cox & Tucker (1969). In the upper transition region radiative losses due to elements other than H and He dominate, and these estimates are only approximate since they do not take mass flow and particle diffusion into account. However, we consider our solutions to be accurate in the lower transition region, where losses due to H and He indeed greatly dominate. We will recompute the upper transition region of our models in a subsequent paper after obtaining better estimates of the radiative losses for elements other than H and He including the effects of particle diffusion and elemental flows.

After computing the total radiative loss $q_R(z)$ we calculate $F_R(z)$, the integral of this quantity from the lower boundary

of our energy balance calculation, z_0, out to the given height z. This integral corresponds to the total radiative energy that is lost between z_0 and z.

As in FAL90, FAL91, and FAL93, we locate this lower boundary at the top of the chromosphere where the transition region is assumed to start. The height z_0 is obtained from observational constraints and cannot be derived from theory because it depends entirely on the details of chromospheric heating that are not yet well understood. Thus, the temperatures at heights below z_0 are those given by our semiempirical model C described above. We compute the temperature stratification above z_0 by requiring that the downward heat transport balances the radiative losses (minus any mechanical dissipation; see below) or equivalently that the decrement of the total heat flux is equal to the value of F_R mentioned above (minus any mechanical energy). The values of the height and temperature at our chosen boundary are $z_0 = 2163.25$ km and $T_0 = 9530$ K.

Our procedure includes an ad hoc mechanical energy dissipation (or heating) term q_M that is assumed to have the form

$$q_M = C_q n_{\rm H} + U \frac{dp}{dz} , \tag{38}$$

where C_q is a coefficient chosen to account for the mechanical energy dissipation other than that due to the mass flow. The second term on the right-hand side of equation (38) represents the mechanical energy dissipation due to the flow (see eq. [A21] in FAL90). However, our method is not limited to the form assumed in equation (38), and it can handle other expressions for the mechanical dissipation. The mechanical energy dissipation term is also integrated from the lowest boundary of our energy balance calculation z_0 to obtain the mechanical energy flux $F_M(z)$ dissipated between the heights z_0 and z.

We find that for the cases shown here, introducing q_M as in equation (38), with the coefficient C_q chosen in such a way as to compensate for the upper chromospheric radiative losses, has effects on lower transition region models that vary in each case (i.e., depending on the mass flow considered). Here we want to show only the effects of velocity without introducing the further complication of variable mechanical heating since in many cases (inflows, the static case, and small outflows) a value of C_q that would account for the upper chromospheric radiative losses has no significant effect on the lower transition region. Thus, in this section we have confined ourselves to cases with $C_q = 0$. We do not include models with outflows larger than those indicated in the next section because such cases indeed require much larger chromospheric heating that would have a significant effect on the lower transition region. In a later paper we will consider nonzero values of C_q and show the effects of mechanical heating on the lower transition region, especially in cases of large outflow.

The total heat flux F_h is defined here as the sum of heat conduction, ionization energy transport, and enthalpy transport terms as we show below. The energy balance requirement (from FAL91, eqs. [9]–[12]) takes the form

$$F_E = F_h(z) + F_R(z) - F_M(z) , \tag{39}$$

where F_E is the constant value that results from the specified lower boundary condition and is equivalent to the total heat flux at the lower boundary z_0. This energy balance equation is sometimes formulated by equating to zero the divergence of the right-hand side of equation (39) (or the derivative with respect to z in our one-dimensional modeling), which is equivalent to the integral form shown here.

The total heat flux F_h can be expressed as

$$\begin{aligned} F_h &= F_T + F_U , \\ F_T &= -\kappa \frac{d \ln T}{dz} + \frac{5}{2} n_e k T v_e \\ &\quad + \sum_{i,k} n_{ik} \left(\frac{5}{2} kT - E_{\rm ion} \right) (v_{ik} + v_k) , \\ F_U &= \frac{5}{2} n_e k T U + \sum_{i,k} n_{ik} \left(\frac{5}{2} kT - E_{\rm ion} \right) U \\ &= \frac{5}{2} pU - U \sum_{i,k} n_{ik} E_{\rm ion} , \end{aligned} \tag{40}$$

where F_T is the thermally driven heat flux, F_U is the mass flow–driven heat flux, $E_{\rm ion}$ is the ionization energy for element k from ionization stage i to the fully ionized stage, κ is the coefficient of heat conduction, and the other symbols have their previous meaning. (Note that for the heat conduction we use the logarithmic temperature gradient rather than the plain gradient.) In these equations we assume that the electric current is zero, which implies that the electron diffusion velocity v_e has the same value as the sum of the diffusion velocities of all hydrogen and helium ions weighted by their charge. The zero electric current condition leads to a "thermoelectric" field (see MacNeice, Fontenla, & Ljepojevic 1991), which is implicitly included in all our calculations. Since we apply these equations at heights above the chromosphere, the ions of elements other than H and He can be neglected for the purpose of computing v_e.

The terms in F_h that contain $E_{\rm ion}$ are called "reactive heat flux" terms; those in F_T are thermally driven, and those in F_U are velocity driven. The equations for F_T and F_U can be elaborated using the expression for v_e and the definition of the mass flow F_m so that

$$\begin{aligned} F_T = F_{\rm cond} &+ \tfrac{5}{2} kT \sum_{i,k} n_{ik} (v_{ik} + v_k) q_i \\ &+ \tfrac{5}{2} kT \sum_k n_k v_k + F_{T\rm react} . \end{aligned} \tag{41}$$

Here $F_{\rm cond} = -\kappa d \ln T / dz$ is the conductive heat flux, q_i is the electric charge of the ionization stage i (in units of the proton charge), and

$$F_{T\rm react} = - \sum_{i,k} n_{ik} E_{\rm ion} (v_{ik} + v_k) \tag{42}$$

is the thermally driven reactive heat flux. Furthermore,

$$F_U = \frac{5}{2} \frac{p}{\rho} F_m + F_{U\rm react} , \tag{43}$$

where

$$F_{U\rm react} = -U \sum_{i,k} n_{ik} E_{\rm ion} = - \left(\frac{F_m}{\rho} \right) \sum_{i,k} n_{ik} E_{\rm ion} \tag{44}$$

is the velocity-driven reactive heat flux.

Our method for determining the temperature structure using the energy balance equation (39) assumes that the

thermally driven heat flux F_T can be expressed as a coefficient times the logarithmic temperature gradient. This is plainly true for the heat conduction term and is approximately true for the other terms because they depend on the diffusion velocities. The diffusion velocities are also driven by the temperature gradient: directly in the case of thermal diffusion, and indirectly in the case of ionization gradients. Thus, in the transition region the dependence of the thermal heat flux F_T on temperature can be described by

$$F_T = -K(z)\frac{d\ln T}{dz}\ , \tag{45}$$

where the coefficient K is obtained by dividing F_T (computed in detail from eq. [41]) by the logarithmic temperature gradient. In our earlier papers we called K the "effective" heat transport coefficient.

The first term in equation (43) for F_U varies because the ratio of gas pressure to mass density, related to the sound speed, varies as the temperature changes; however, the second term has a stronger variation because it depends on the H and He ionization changes. Although these variations are due to the temperature variation, F_U cannot be expressed as a linear function of the logarithmic temperature gradient. We take F_U as given in our procedure for correcting the height scale and recompute it in each iteration of the overall procedure.

After computing the radiative losses, energy fluxes, K, and F_U, we adjust the position of each point of our height grid, stretching or compressing the intervals between adjacent points in such a way that equation (39) is satisfied at all heights in the transition region. For this, we start at z_0 and step outward, recomputing the position of each height point so that the height interval from the adjacent lower point, Δz, satisfies the following equation:

$$-K_{i-1/2}\frac{\Delta\ln T}{\Delta z} + F_{Ui-1/2} = F_E - (F_R - F_M)_i - \frac{\Delta z}{2}(q_R - q_M)_{i-1/2}\ , \tag{46}$$

where the index i is that of the lower point of the interval in question and the values with the index $i-\frac{1}{2}$ are the mean values of that interval. Note that the sum of the terms on the right-hand side is equal to $F_E - (F_R - F_M)_{i-1/2}$ and that the sum of the terms on the left-hand side is $(F_h)_{i-1/2}$. Thus, this equation is a numerical approximation of equation (39) evaluated at the center of the interval. As the calculation proceeds outward to the next interval, the value of $(F_R - F_M)_{i-1}$ is recomputed incrementally,

$$(F_R - F_M)_{i-1} = (F_R - F_M)_i + \Delta z(q_R - q_M)_{i-1/2}\ . \tag{47}$$

Equation (46) is quadratic in Δz, and in solving it we select the sign of the square root term in the solution so that Δz is positive, which often implies that a different sign must be chosen depending on the sign of F_U. We avoid numerical cancellations that can arise when the velocities are large or near zero because we use asymptotic expressions in such situations.

This scheme for computing a revised height grid is nested in a procedure consisting of the following steps: compute corrections for Δz, apply numerical damping to the computed corrections, construct the revised height grid, and recompute the fluxes using the same K, F_U, q_R, and q_M. This height grid revision procedure is iterated 3 times (unless the changes are negligible). The numerical damping mentioned above is just a standard procedure to avoid unphysical oscillations in the solution of the highly nonlinear equation; it does not affect the final result and just makes the solution easier to obtain.

Then we recompute the ionization and the non-LTE radiative transfer equations as described in the earlier sections. We recompute the radiative losses, energy fluxes, and the coefficient K and solve equation (46) again as described above. This procedure converges uniformly and has the virtue of simplicity, since the "effective heat transport coefficient" K hides the complicated dependencies on the temperature gradient. This method has served us well in building a grid of models incrementally, enabling us to start the computation of a new model by using another one with a different particle flux.

5. EFFECTS OF VELOCITIES ON THE ATMOSPHERE

We now discuss the results obtained for a set of models illustrating six cases of hydrogen particle flow, $F_{\rm H}$: outflows of 2×10^{15} and 1×10^{15} particles cm^{-2} s^{-1}; zero flow; and inflows of -1×10^{15}, -5×10^{15}, and -10×10^{15} particles cm^{-2} s^{-1}. We refer to this sequence of six models by the names out2, out1, 0, in1, in5, and in10, respectively. Table 1 shows the logarithmic gradients of T and n_p/n_a at two temperature values, 2×10^4 and 10^5 K.

Figure 1*a* shows the calculated $T(z)$ structures in the low transition region, and Figure 1*b* shows the $T(z)$ structures at greater heights in the upper transition region and the low corona. Clearly, the flow velocities considered here strongly affect the energy balance temperature structure throughout the transition region and low corona.

Inflows lead to much smaller temperature gradients as a result of the much smaller need (or no need) of thermally driven heat transport to support the radiative losses. Large inflow velocities lead to an extremely extended transition region in which the variation in energy transported down-

TABLE 1

LOGARITHMIC GRADIENTS OF T AND n_p/n_a (IN cm^{-1}) AT $T = 2\times10^4$ AND 10^5 K

Model	$F_{\rm H}$ (cm^{-2} s^{-1})	$d\log T/dz$ at $T=2\times10^4$ K	$d\log(n_p/n_a)/dz$ at $T=2\times10^4$ K	$d\log T/dz$ at 10^5 K	$d\log(n_p/n_a)/dz$ at 10^5 K
in10.....	-10×10^{15}	4.76×10^{-7}	2.61×10^{-6}	8.23×10^{-8}	2.00×10^{-7}
in5.....	-5×10^{15}	1.07×10^{-6}	5.64×10^{-6}	1.57×10^{-7}	3.83×10^{-7}
in1.....	-1×10^{15}	4.43×10^{-6}	1.07×10^{-5}	3.22×10^{-7}	7.96×10^{-7}
0.....	0	6.26×10^{-6}	1.05×10^{-5}	4.59×10^{-7}	1.24×10^{-6}
out1	1×10^{15}	7.59×10^{-6}	1.13×10^{-5}	6.70×10^{-7}	3.79×10^{-6}
out2	2×10^{15}	1.00×10^{-5}	1.12×10^{-5}	8.84×10^{-7}	9.90×10^{-6}

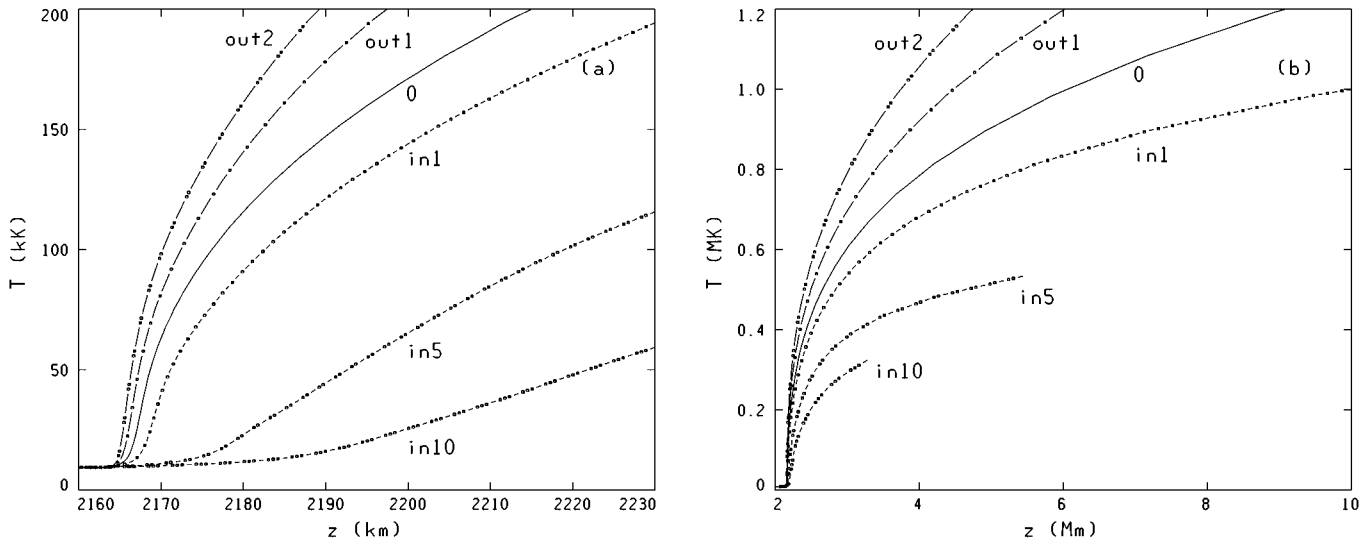

FIG. 1.—Calculated temperature distributions (*a*) in the lower transition region and (*b*) extending into the corona, for the six models out2, out1, 0, in1, in5, and in10. The upper temperature limits are chosen to keep the flow velocities subsonic.

ward by the mass flow through each large height interval is dissipated by the radiative losses in that interval. At such shallow temperature gradients the thermally driven heat flux F_T is negligible (Fig. 2 illustrates this behavior), and the diffusion effects are also negligible. An analytic solution of equation (13) is then possible (see Appendix C).

The opposite is true for outflows. The temperature gradient must increase as the outward mass flow increases so that the inward thermally driven heat transport variation can compensate for the large variation of the velocity-driven outward energy flow and the radiative losses.

Note that our statements regarding $T(z)$ apply only to the transition region and lower corona. In coronal layers above those considered here the effect of mechanical dissipation becomes very important, and the effects of velocity reverse themselves at heights beyond the temperature maximum in the corona because then the energy flow by particle outflows has a direction opposite to that of the temperature gradient. Thus, outflows cause a thinner transition region with the corona closer to the chromosphere but then a more extended high corona where the temperature is over a million degrees. Of course, this is true only if the boundary condition at the top of the chromosphere remains the same and the coronal heating increases accordingly.

Figure 2 shows the total heat flux, F_h, and its velocity-driven component, F_U (see eq. [40]). For outflows, F_U is positive but, as a result of the very steep temperature gradient, overpowered by the negative F_T in the very thin transition region. For small flow velocities (out2 to in1), the total heat flux is almost the same at temperatures below about 10^5 K and is about -2×10^5 ergs cm^{-2} s^{-1} at that temperature, regardless of F_U (which has the same sign as the particle

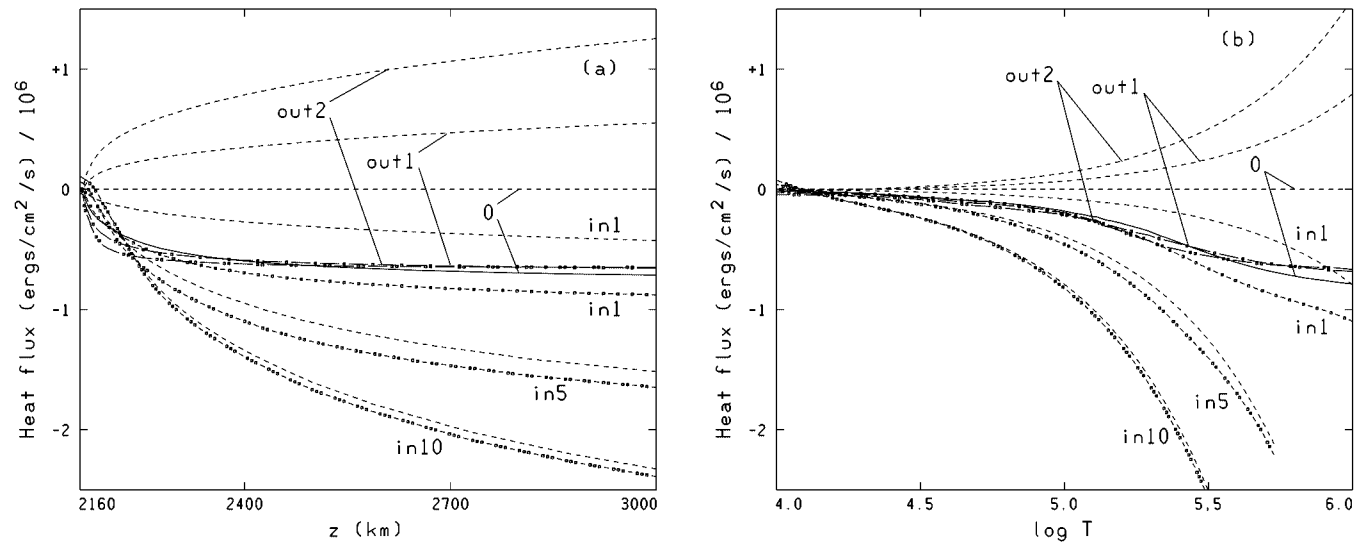

FIG. 2.—Total heat flux F_h (*curves with dots and short and long dashes*, as in Fig. 1) and its velocity-driven component F_U (*dashed curves*), from eq. (40), vs. z and vs. T.

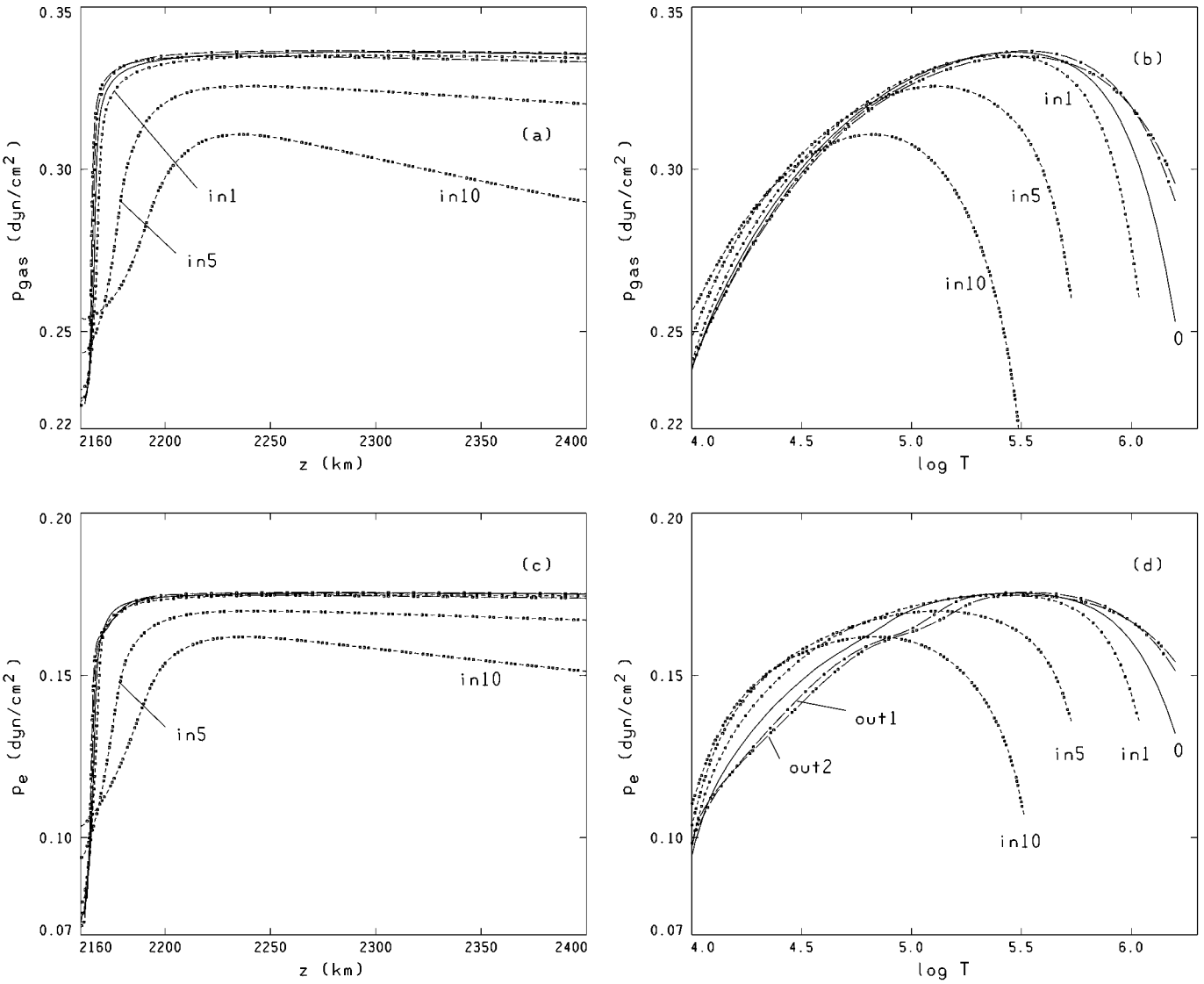

FIG. 3.—p_{gas} and p_e vs. z and vs. T

flow). For large inflows the curves diverge, and the heat flux at 10^5 K for the in10 case is about 4 times larger (in absolute value) than for small flows.

Figure 3 shows the gas pressure and electron pressure contributions in the models. The gas and electron pressures reach a local minimum at the top of the chromosphere below the abrupt temperature increase and the slightly less significant density decrease in the transition region. The gas pressure is not monotonic because of the contribution of the "turbulent pressure" term in equation (37). The rapid decrease in ρ produces a rapid decrease in the "turbulent pressure term" that forces the gas pressure to increase slightly in order to satisfy the momentum balance equation. The "total pressure" p_{total} in equation (37) decreases monotonically with height, as shown in Figure 4 for the in1 model. In the chromosphere, the gas pressure has a more gradual decrease with height, and the base of the transition region occurs at a greater height, than would be calculated in hydrostatic equilibrium without the turbulent pressure term (see eq. [37]).

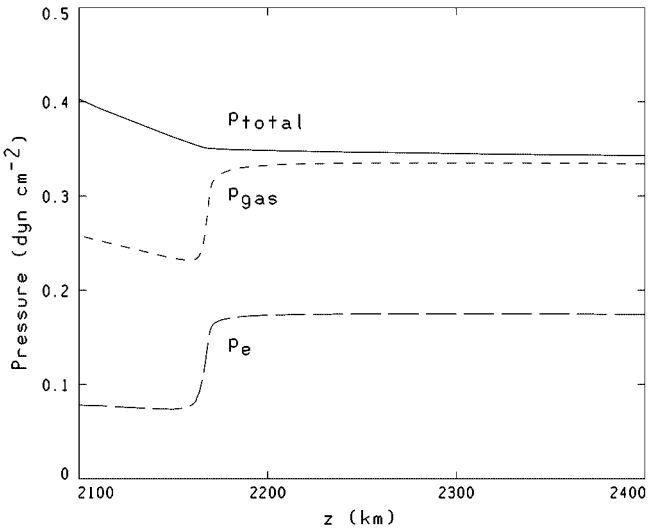

FIG. 4.—p_e, p_{gas}, and p_{total} vs. z for model in1

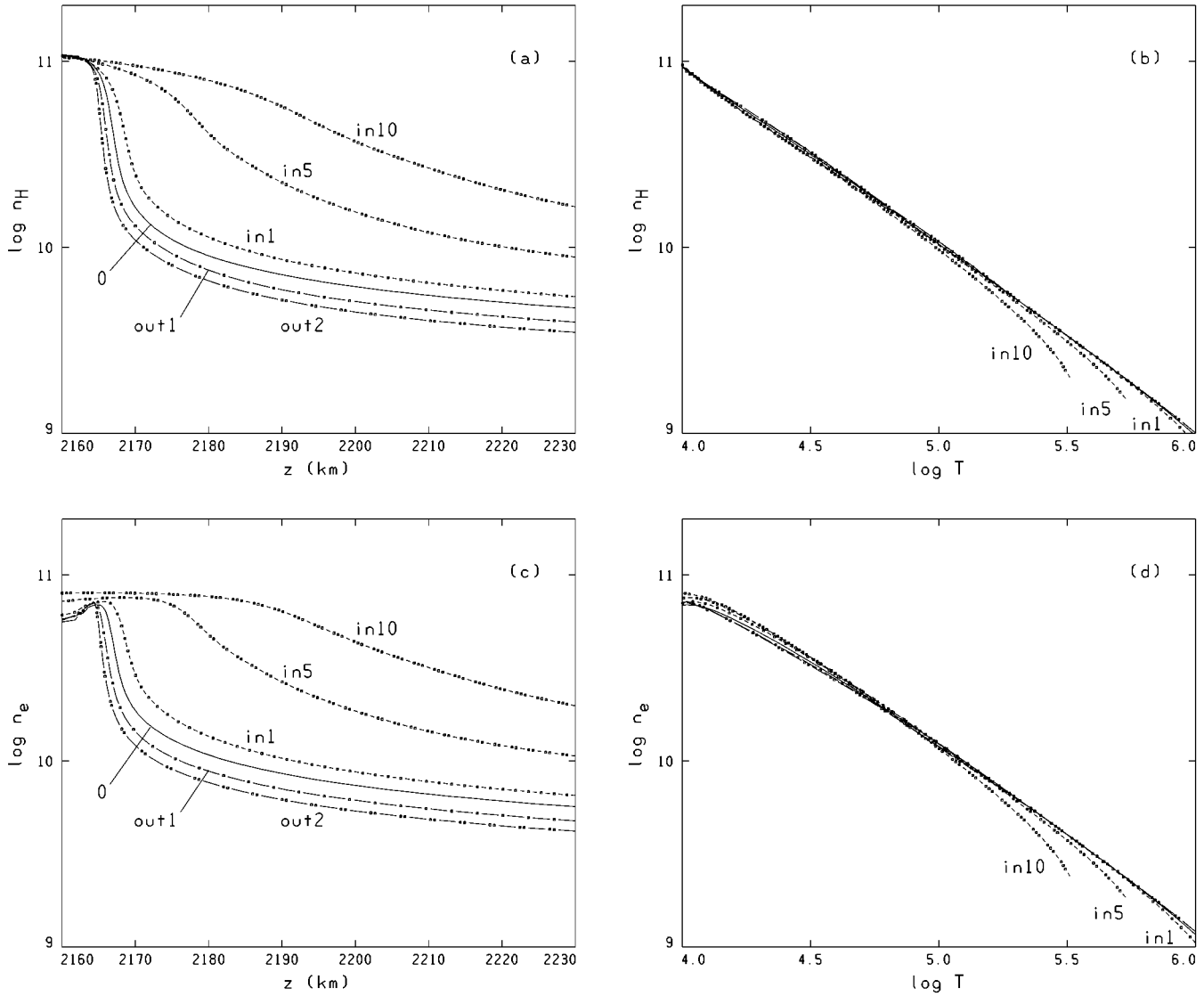

FIG. 5.—n_H and n_e vs. z and vs. T

Figures 5*a* and 5*c* show n_H and n_e as functions of height for all the models. The differences between these curves are mainly due to the different $T(z)$ structures of the models. As shown in Figures 5*b* and 5*d*, n_H and n_e as functions of T are about the same for all the models, except near the upper boundary where the flow approaches the sound speed.

Figures 6*a* and 6*b* show the neutral hydrogen fraction, y_a, as functions of z and T. As usual, diffusion increases y_a as a function of T, but y_a is further enhanced by the transport of neutral H due to outflows. The curves in Figure 6*b* tend to converge at lower temperatures because the back-radiation in the energy balance cases is not severely affected by the flow (as we show below). For the large inflows in Figure 6*b* the temperature gradient is so small that diffusion becomes negligible and y_a depends only on temperature regardless of the flow.

Figures 6*c*–6*f* show y_α and y_β as functions of z and T. The behavior of $y_\alpha(T)$ resembles that of $y_a(T)$ at lower temperatures, but at higher temperatures y_α is much larger for outflows than for inflows. Figures 6*d* and 6*f* show that the effects of flow velocities are much more pronounced for He II than for He I. Our He II ionization equilibrium calculations include the effects of dielectronic recombination, based on rate coefficients given by Romanik (1988). Dielectronic recombination from He II to He I greatly exceeds radiative recombination for temperatures higher than 10^5 K and causes y_α to be more than 10 times larger in this temperature range than would be calculated with radiative recombination alone. However, the He I density in the upper transition region is still very small.

Figure 7 shows the total diffusion velocities of H atoms and ions (protons), $v_a + v_H$ and $v_p + v_H$, respectively. However, note that we neglect the relative diffusion velocity between H and He, so that $v_H = v_{He} = 0$. These velocities are substantial for the outflow and the static models; they are still significant for the inflow model in1 but are negligible for in5 and in10 since the temperature and ionization gradients are very small in these cases.

Figure 8 shows the helium diffusion velocities v_α and v_β. Comparison with our fixed $T(z)$ calculations indicates that the changes in $T(z)$ due to energy balance tend to increase He diffusion for outflows and decrease it for inflows.

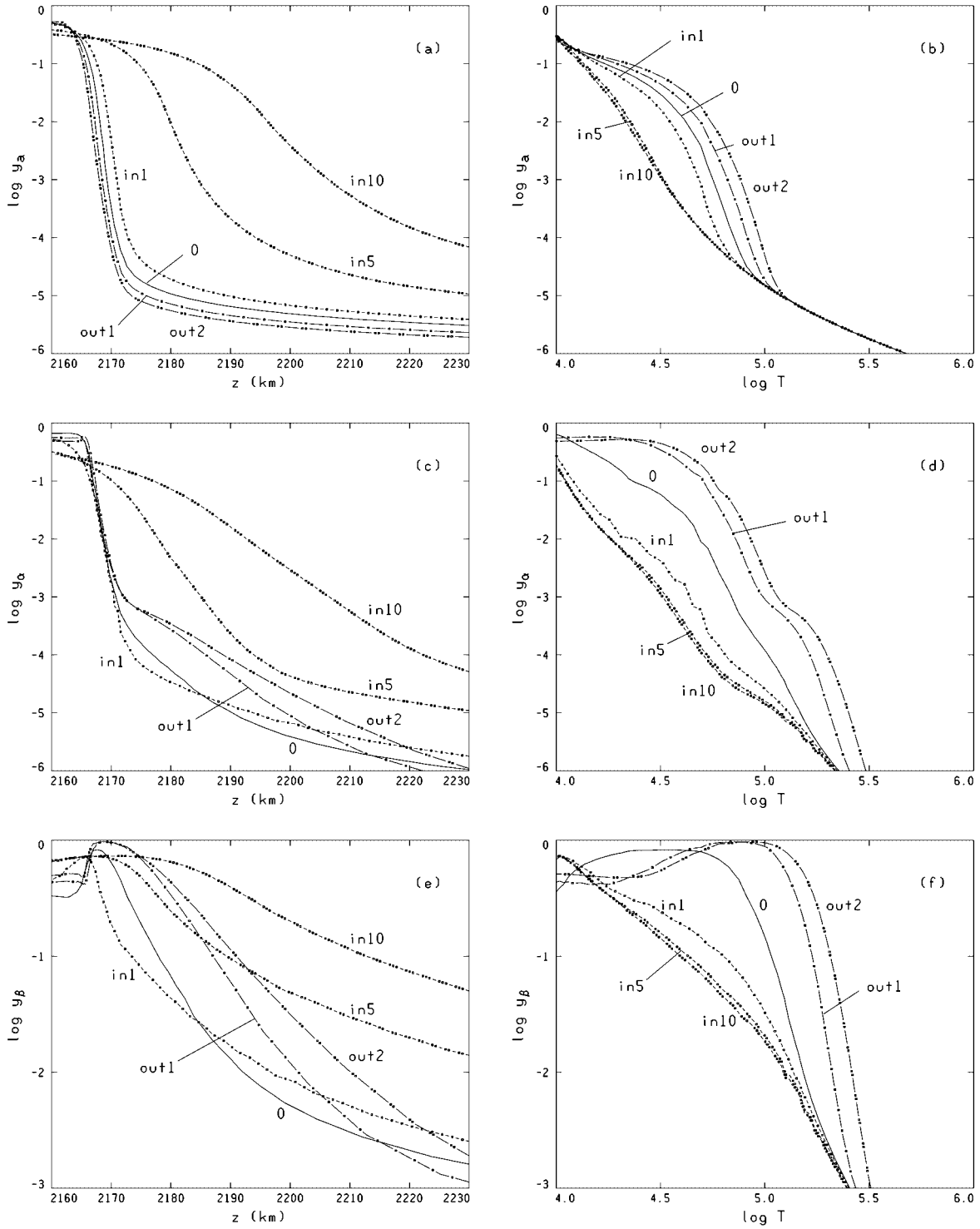

FIG. 6.—y_a, y_α, and y_β vs. z and vs. T

Figure 9 shows the reactive components of the energy flow (see § 4) pertaining to H and He ionization energy transport. We show $F_{U\text{react}}$ from equation (44) (*dashed curves*) due to the mass flow alone and the sum

$$F_{\text{react.total}} = F_{U\text{react}} + F_{T\text{react}} , \qquad (48)$$

representing the "total reactive energy flow" that includes both mass velocity and particle diffusion effects. Figures 9*a* and 9*b* show these quantities for H as a function of z and T, respectively. These figures show that for H the temperature-driven part (due to diffusion) dominates in the outflow models, static models, and for in1 but is small for in5 and negligible for in10. The particle diffusion effect is much less important for He I as shown in Figures 9*c* and 9*d*, and it is negligible for He II (Figs. 9*e* and 9*f*). The He temperature-driven reactive energy flux is negligible in most cases (except for the static model) because it is overbalanced by the He II reactive velocity-driven energy flux.

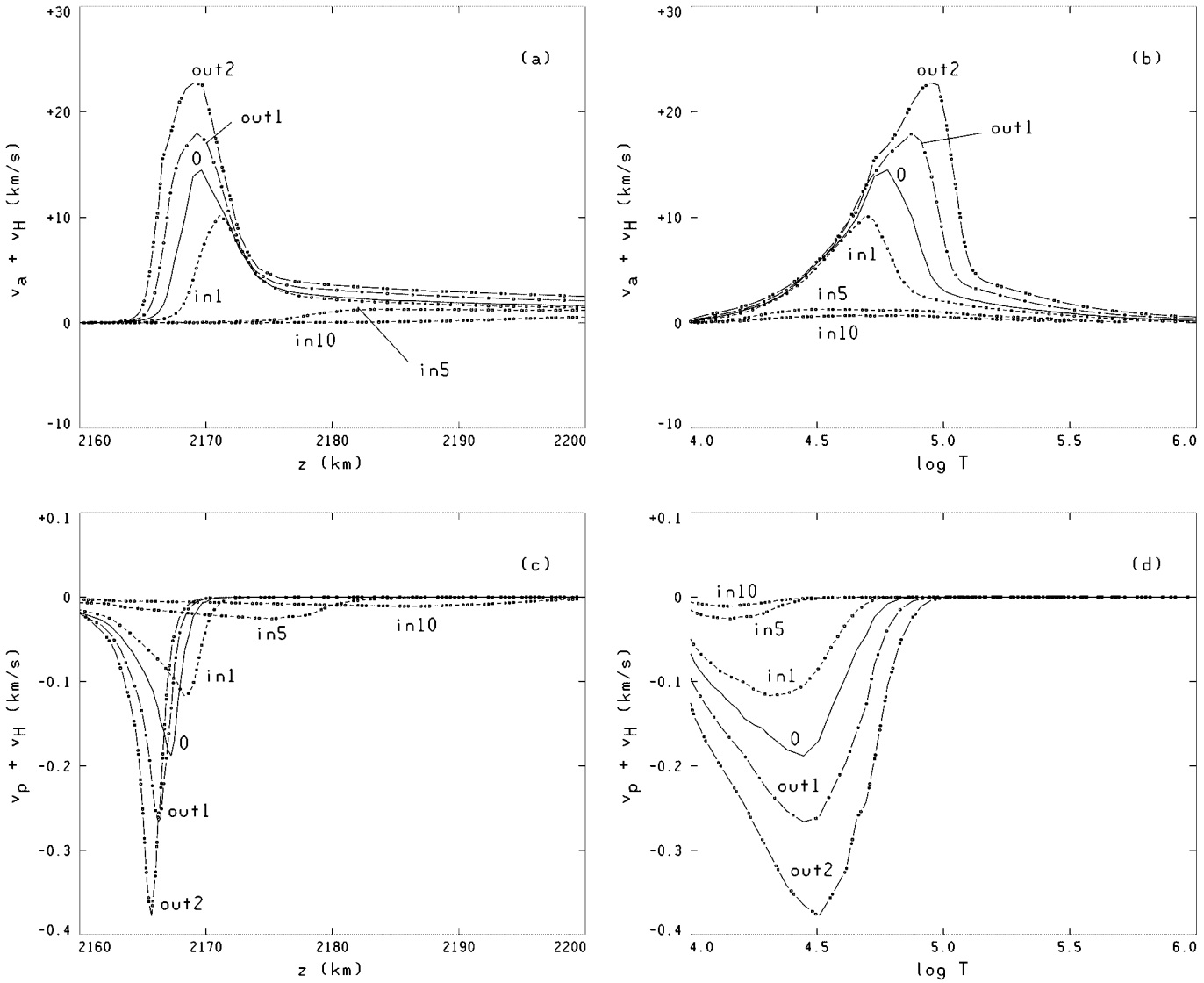

FIG. 7.—Total diffusion velocity of H atoms and protons $v_a + v_H$ and $v_p + v_H$ vs. z and vs. T

The temperature-driven H reactive energy flux plays a major role in the low transition region of all the models except in5 and in10. The values of $F_{U\text{react}}$ and $F_{\text{react.total}}$ are shown in Table 2 for 2×10^4 K and in Table 3 for 10^5 K. These tables also list the values of F_h and F_{cond} (eqs. [40] and [41]) and the height above z_0, the base of the transition region, in each model. In the large inflow cases the enthalpy energy flow becomes dominant and so large that radiative losses are only able to dissipate this energy within a layer of large extent. This leads to very shallow temperature gradients and very extended transition regions in these cases.

Figure 10 shows the total radiative losses q_R as functions of z and T. Figure 10*a* shows that in most cases these radiative losses are sharply peaked in the transition region, but this peak shifts to greater heights, and broadens, for inflows. The opposite is true for outflows. Figure 10*b* shows that the large inflow cases practically share a common curve (except for some departure at high temperature) and have a very flat maximum. In models with small inflow and with outflow the H and He peaks become bigger and shift to large temperatures as the flow increases; this behavior is typical of the effects of particle diffusion. We also note that at temperatures near 10^4 K the large inflow models, due to the H contribution, have larger radiative losses than all the others, but these radiative losses are not very large in absolute value [although in these shallow $T(z)$ cases they occur over a large height range and accumulate to significant values].

Figures 10*c* and 10*d* show the radiative losses scaled differently, in ways commonly used in the literature. They show the same basic behavior as Figure 10*b*. At temperatures above 4×10^5 K the radiative losses shown in Figure 10*c* are almost the same for all models, but this is just due to our assumption that the function $q_R/(n_e n_H)$ as given by Cox & Tucker (1969) accounts for the radiative losses due to all elements other than H and He. This assumption is probably not accurate (see Dupree, Moore, & Shapiro 1979) because diffusion and flows would produce the same effects on other species (although for ions the diffusion effects are probably not large). At lower temperatures where the H and He radiative losses dominate, these functions are different for all the models, thus showing that none of the customary scaling laws apply for cases with flows. A different case is that of

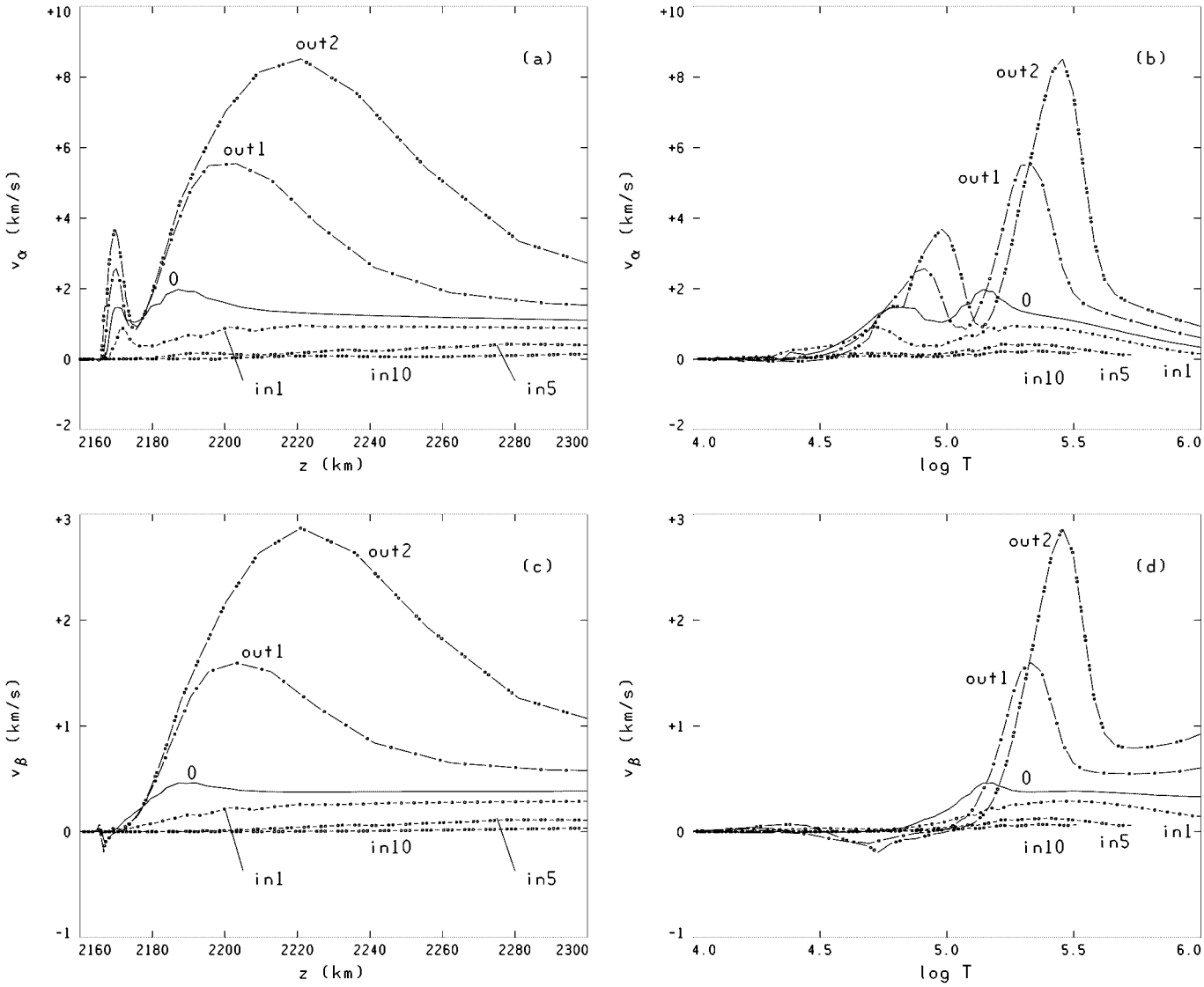

FIG. 8.—v_α and v_β vs. z and vs. T

large inflows for which Figure 10 shows that the radiative loss versus T follows a common curve.

5.1. *Effects of Velocities on the Line Profiles*

In this paper we are not concerned with fitting any particular observations but only with showing the physical effects of the combined diffusion and mass flow processes on the H and He ionization and line formation. We do not include models in which the chromospheric and photospheric portions correspond to active regions or other specific solar features. These are postponed to a later paper where we will include mechanical energy dissipation in addition to the dissipation caused by the particle flow that we consider here. Given these limitations, we note how our results compare with available observations of high spectral, temporal, and spatial resolution, to indicate where our results are generally consistent with the behavior of observed lines and to show where some problems still remain.

Figures 11*a* and 11*b* show the Lyα profiles for the inflow and outflow cases, respectively. In the inflow cases the lines become slightly broader and the peak intensities increase with increasing flow, producing an increase in the integrated line intensity and peak-to-center ratios as large as $\sim$4. Asymmetries only start to become substantial for large inflows (for in10 the blue peak is larger than the red peak). In the outflow cases the peak intensities increase very little but the central intensity increases with increasing flow (thus also producing an increase in the integrated intensity, but for a different reason). For outflows the relative central reversal becomes smaller and the peak-to-center ratio may drop as low as 1.2. For outflows the asymmetry remains small and manifests itself as a slight increase of the red peak as the deepest point of the central reversal moves very slightly to the blue. This asymmetry is so small that it may be hard to detect in observations.

These changes in line profiles arise for different reasons in inflows and outflows. For inflows the diffusion effects become smaller as the flow increases, and for large inflows they become insignificant. This drives the region of formation of the line center deeper in the atmosphere where the temperature is lower than in the static case but where the

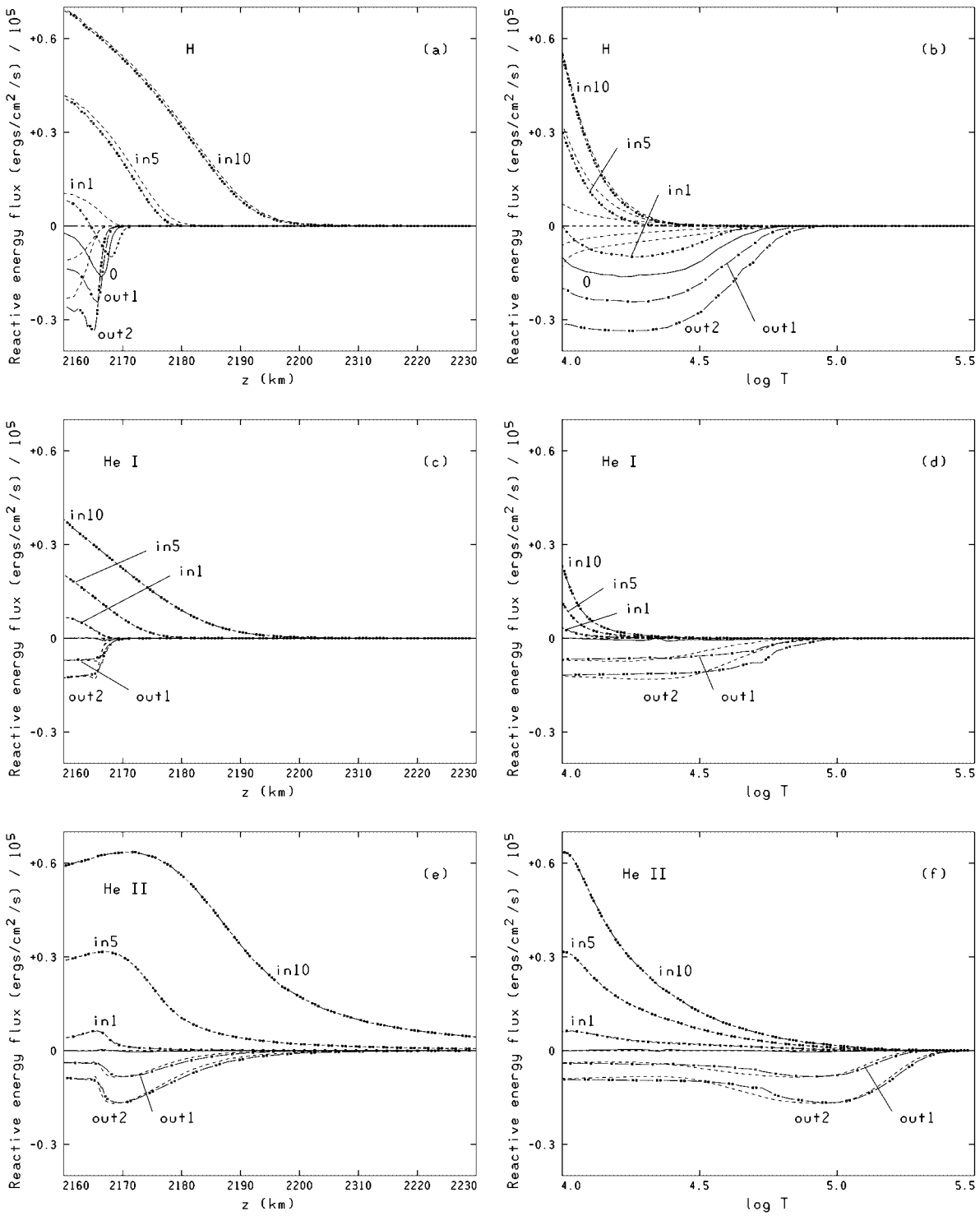

FIG. 9.—H, He I, and He II components of $F_{U\text{react}}$ (*dashed curves*) and $F_{\text{react.total}}$ (*curves with dots and short and long dashes*, as in Fig. 1) vs. z and vs. T. See eqs. (42), (44), and (48).

line source function is enhanced because the electron density is higher, thus producing a moderate decrease at line center, except for model in10 where there is a moderate increase at line center. The peaks form at the top of the chromosphere (at 10^4 K or less) where diffusion effects are small in all cases; thus, the increased peak intensities are just due to the larger electron density and amount of material at this temperature. For outflows, on the other hand, diffusion effects increase and shift the region of formation of the line center to a layer that is thinner but has temperatures of $\sim 3 \times 10^4$ K or more, while the line peaks still form at about the same temperature and electron density as in the static case.

This behavior of the computed Lyα line is consistent with the very detailed observations by FRT88, who found that the relative depth of the central reversal of this line changes with position (unfortunately, appropriate time sequences

TABLE 2
HEAT FLUX AND ITS COMPONENTS AT $T = 2 \times 10^4$ K

Model	$z - z_0$ (cm)	F_h (ergs cm^{-2} s^{-1})	$F_{\rm cond}$ (ergs cm^{-2} s^{-1})	$F_{U\rm react}$ (ergs cm^{-2} s^{-1})	$F_{\rm react.total}$ (ergs cm^{-2} s^{-1})
in10.....	3.11×10^6	-1.28×10^5	-9.02×10^2	2.96×10^4	2.90×10^4
in5.....	1.53×10^6	-6.65×10^4	-2.04×10^3	1.55×10^4	1.37×10^4
in1.....	4.96×10^5	-3.43×10^4	-8.76×10^3	4.57×10^3	-6.83×10^3
0.....	3.44×10^5	-3.33×10^4	-1.23×10^4	0	-1.60×10^4
out1	2.53×10^5	-4.27×10^4	-1.52×10^4	-1.30×10^4	-3.48×10^4
out2	1.93×10^5	-5.51×10^4	-2.00×10^4	-2.63×10^4	-5.43×10^4

were not available). While the observed average quiet Sun profile and absolute intensity are in reasonable agreement with the static models (see FAL90), FRT88 showed that some quiet Sun profiles have deeper and others have shallower central reversals than the average. This effect is larger in active regions where intense peaks are sometimes observed at some locations, while at other locations in active regions the central reversal of the line is almost filled in. Of course, in active regions the line is generally more intense (see FRT88 and the FAL papers) since their chromospheric temperature and heating are larger. Regardless of these intensity differences, the processes described here, whereby the peak-to-center ratio grows larger with inflows and decreases with outflows, appear to be consistent with observations. (For example, Fig. 6 of FRT88 shows two profiles whose central reversals are very different, and in Fig. 8 of that paper the inflow profile c has a much deeper reversal than the outflow profiles b and d.)

Figures 11*c* and 11*d* show the Lyβ profiles for the inflow and outflow cases, respectively. The outflow profiles (Fig. 11*d*) show increasing intensity as the flow increases. This is again due to the increased effects of diffusion that drive the line-center formation region up to temperatures of $\sim 3 \times 10^4$ K; the effect of this higher temperature overpowers the reduction in the thickness of the region of line formation. The inflow profiles (Fig. 11*c*), instead, show a slight decrease of intensity for small inflows due to the shift of the line-center formation region toward lower temperatures because of the reduction of diffusion effects. With large inflows the line becomes stronger and wider than in the static case as a result of the increasing optical thickness of the line-emitting region. There are no pronounced asymmetries, but clearly the line center is shifted slightly to the red with inflows and to the blue in the static case, while the outflow cases show increasing blueshift.

The Lyβ line profiles observed by *SOHO* (Warren, Mariska, & Wilhelm 1998) show a peak intensity of -2000 ergs cm^{-2} s^{-1} sr^{-1} Å^{-1} and integrated intensity of $\sim$900 ergs cm^{-2} s^{-1} sr^{-1} (or $\sim$800 when the local continuum is removed), and these values are consistent with our current static model. However, the Lyβ profile observed by *SOHO* shows a very small but definite asymmetric self-reversal that is not predicted by our present static calculations. This small central reversal contrasts with larger ones reported previously from *OSO 8* data; however, the large reversals observed by *OSO 8* may have been caused by geocoronal absorption at the low orbit of that spacecraft. The relatively low spectral resolution of these data makes it difficult to separate the geocoronal absorption in the way used by FRT88 for Lyα line profiles. In the context of our models, several possibilities remain to account for the small Lyβ central reversal observed by *SOHO*. (1) One likely possibility suggested by FRT88 and Fontenla et al. (1989) is absorption by a "cloud layer" consisting of neutral hydrogen in the lower corona just above the transition region. The spicules observed in Hα are the densest component of such a layer, but, of course, much more material is visible at the limb in Lyα than in Hα, and all this material would absorb in Lyβ. (2) Another likely possibility is that various portions of the observed area are covered by regions of inflow, of outflow, and of stationary material and that a combination of our computed profiles in these cases may produce an apparent self-reversal. (3) It is possible that an unknown blend may cause an apparent self-reversal. However, all higher Lyman lines show a similar, but decreasing, asymmetric self-reversal, and this is hard to explain by blends. (4) It is likely that in most observations the line of sight is not aligned with the temperature gradient so that portions of the sides of our model structures are observed. (5) It is also likely that our chromospheric models need improvement and that such improvements could lead to changes in the shape of the emitted profiles. Note that the above possible explanations (1) and (2) may also account for the asymmetry of the central reversal and its evolution among the higher members of the Lyman series.

The He I line profiles are shown in Figure 12. The behavior of the resonance line with the lowest excited level energy, the 58.4 nm line, is somewhat similar to that of Lyα. With

TABLE 3
HEAT FLUX AND ITS COMPONENTS AT $T = 10^5$ K

Model	$z - z_0$ (cm)	F_h (ergs cm^{-2} s^{-1})	$F_{\rm cond}$ (ergs cm^{-2} s^{-1})	$F_{U\rm react}$ (ergs cm^{-2} s^{-1})	$F_{\rm react.total}$ (ergs cm^{-2} s^{-1})
in10.....	1.07×10^7	-8.24×10^5	-3.23×10^4	1.62×10^3	1.61×10^3
in5.....	5.56×10^6	-4.57×10^5	-6.18×10^4	9.00×10^2	8.90×10^2
in1.....	1.93×10^6	-2.06×10^5	-1.27×10^5	2.86×10^2	2.56×10^2
0.....	1.30×10^6	-1.81×10^5	-1.81×10^5	0	2.74×10^2
out1	9.19×10^5	-1.96×10^5	-2.64×10^5	-7.70×10^3	-7.94×10^3
out2	7.00×10^5	-2.13×10^5	-3.50×10^5	-1.67×10^4	-1.68×10^4

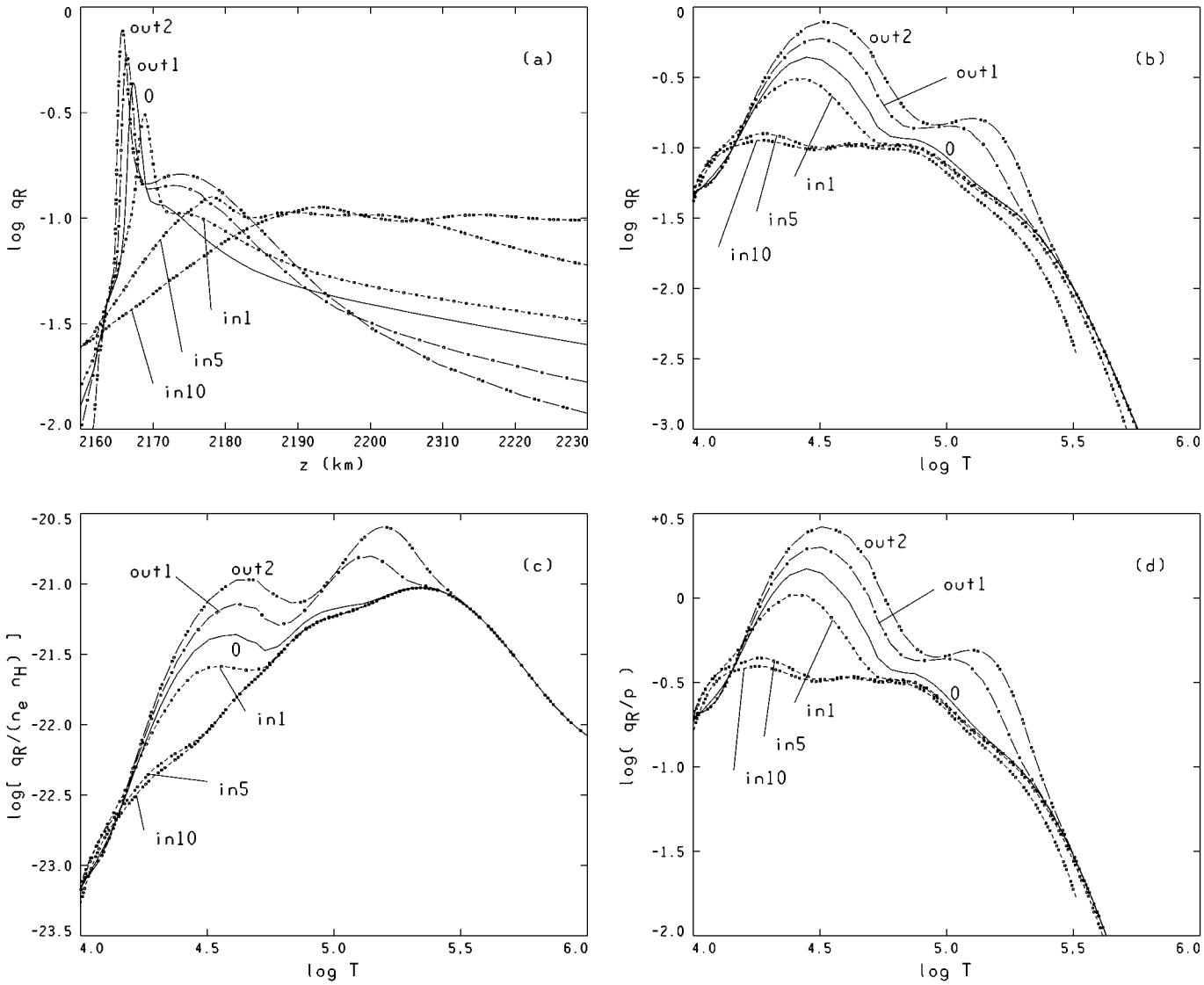

FIG. 10.—q_R vs. z and vs. T; $q_R/n_e n_H$ vs. T; and q_R/p vs. T

increasing inflow the self-reversal becomes more pronounced because the peaks increase more than the line center. However, in contrast with Lyα, with increasing outflow the line center increases very strongly and changes the line's shape from self-reversed to almost pure emission (for out2). The 53.7 nm line behaves similarly; however, (1) it does not have a self-reversal in the static case but a flat top instead, and (2) it develops only a moderate self-reversal with increasing inflow. The infrared absorption line at 108.3 nm deepens with the magnitude of the flow velocity. This strengthened absorption is mainly due to increased optical thickness: for inflows, this is caused by the greater extent of the lower transition region; for outflows, this occurs at the top of the chromosphere where increased UV radiation enhances the population of the triplet ground level as a result of greater He II recombination (see FAL93 and Avrett et al. 1994 for a discussion of how this line is formed).

Unit optical depth at the center of the He I 58.4 nm line occurs at the base of the transition region near $z = 2160$ km, where $T \approx 10^4$ K. Figure 6 shows that, in this region, the values of y_α for inflow and outflow cases are smaller than in the static case and the values of y_β are larger than in the static case. The greater helium ionization in this region leads to enhanced He I line source functions. As shown in Figures 12*a*–12*d* (and in Fig. 13), this produces emission lines for all moving models that are stronger than in the static case. The greater He I ionization does not significantly affect the source function of the He I 1083 nm line but increases the population of the lower level, thus causing greater absorption of the infrared photospheric continuum as shown in Figures 12*e* and 12*f*.

The He II lines shown in Figure 13 behave differently from the H and He I lines. However, their intensities still increase with increasing flow velocity, regardless of its sign, except in the case of model in1. The lowest excitation resonance line, at 30.4 nm, has a flat top in the static case and develops a small self-reversal as the magnitude of the flow velocity increases. For inflows this occurs because, with increasing velocity, the line-center–forming region grows thicker geometrically and moves to lower temperature and higher electron density. For outflows the line intensity increases strongly because the line-forming region occurs at higher

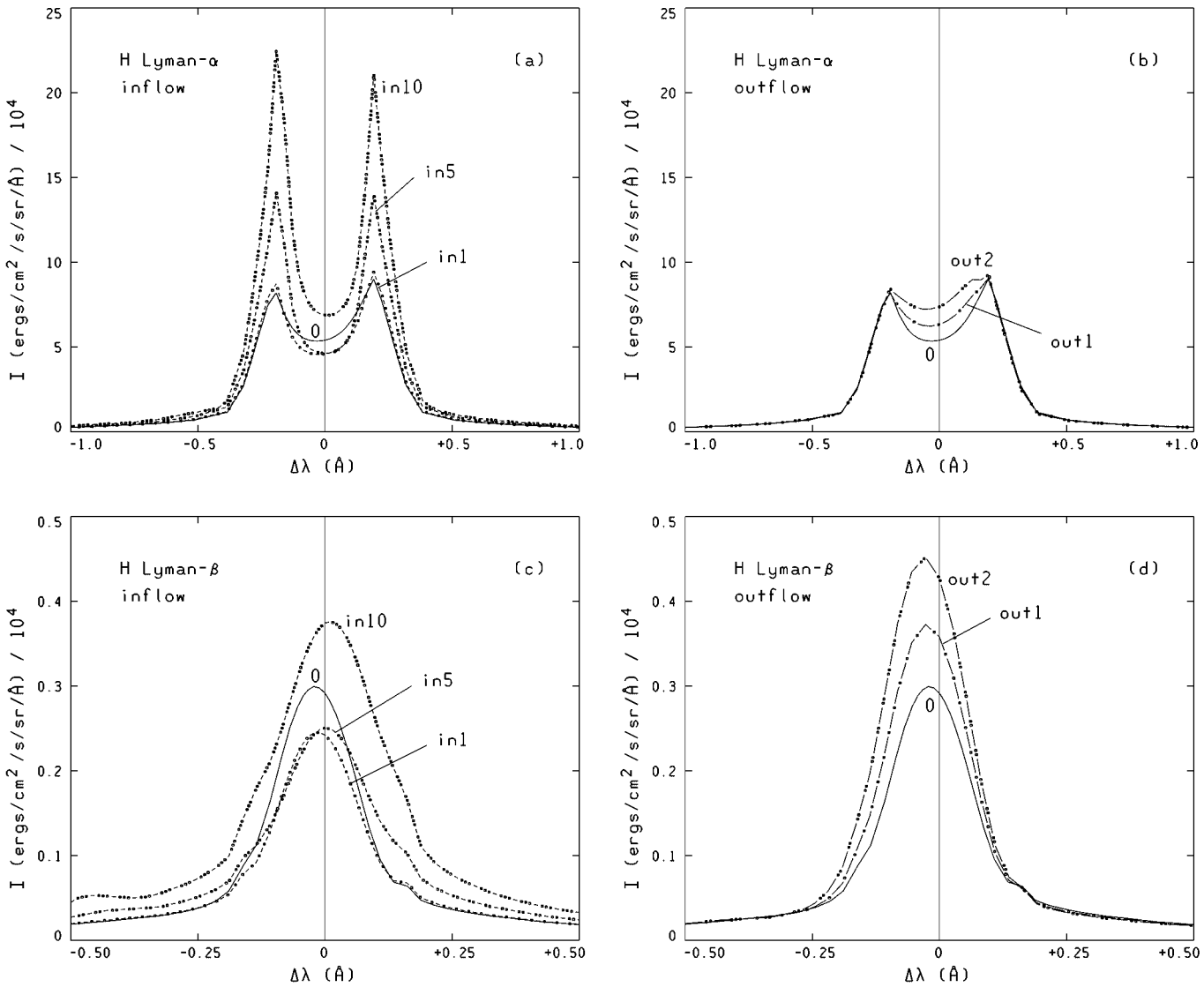

FIG. 11.—Calculated disk center H line profiles

temperatures and this more than compensates for the smaller optical depth.

The He II 25.6 nm line also grows stronger with both increasing inflows and increasing outflows and becomes rather bright for outflows. This line has a typical pure emission profile in all cases. Its center shifts appreciably (even more than Lyβ) since this line forms at greater heights where velocities are larger.

The He II 164.0 nm line grows stronger with both increasing inflows and increasing outflows, but the line shape is flatter for outflows. There are differences between our computed profiles and observations (e.g., Kohl 1977): in our calculations the composite red peak is somewhat larger than the composite blue peak, while the opposite is generally observed. Walhstrom & Carlsson (1994) calculated the 164.0 nm line using model C of VAL81 without diffusion or velocities. They found that at transition region densities the collisional coupling between the three $n = 2$ fine-structure levels and between the five $n = 3$ fine-structure levels is not large enough to populate each group according to their statistical weights and that this results in changes in the shape of the composite 164.0 nm line that lead to closer agreement with the observations. In the present paper, however, we have assumed for simplicity that the two groups of sublevels are populated according to their statistical weights, and this may be the reason for the discrepancy with the observations. In addition, since this composite line is broad, comparison with observations must consider blends with other lines, e.g., Cr II 164.0364 nm, Fe IV 164.037 nm, Fe III 164.0384 nm, and possibly other lines that may blend into the composite red peak.

Our calculations show that, for the moderate flow velocities we consider here, line shifts are so small that they might only be detectable in the relatively weak Lyβ line and the somewhat stronger He II 25.6 nm line. For the largest inflows, our computed blue peaks of the bright and saturated or self-reversed resonance lines of H and He are brighter than the red peaks. However, for small flows both computed peaks are nearly equal and the differences would be undetectable. Consequently, the line shift and asymmetry

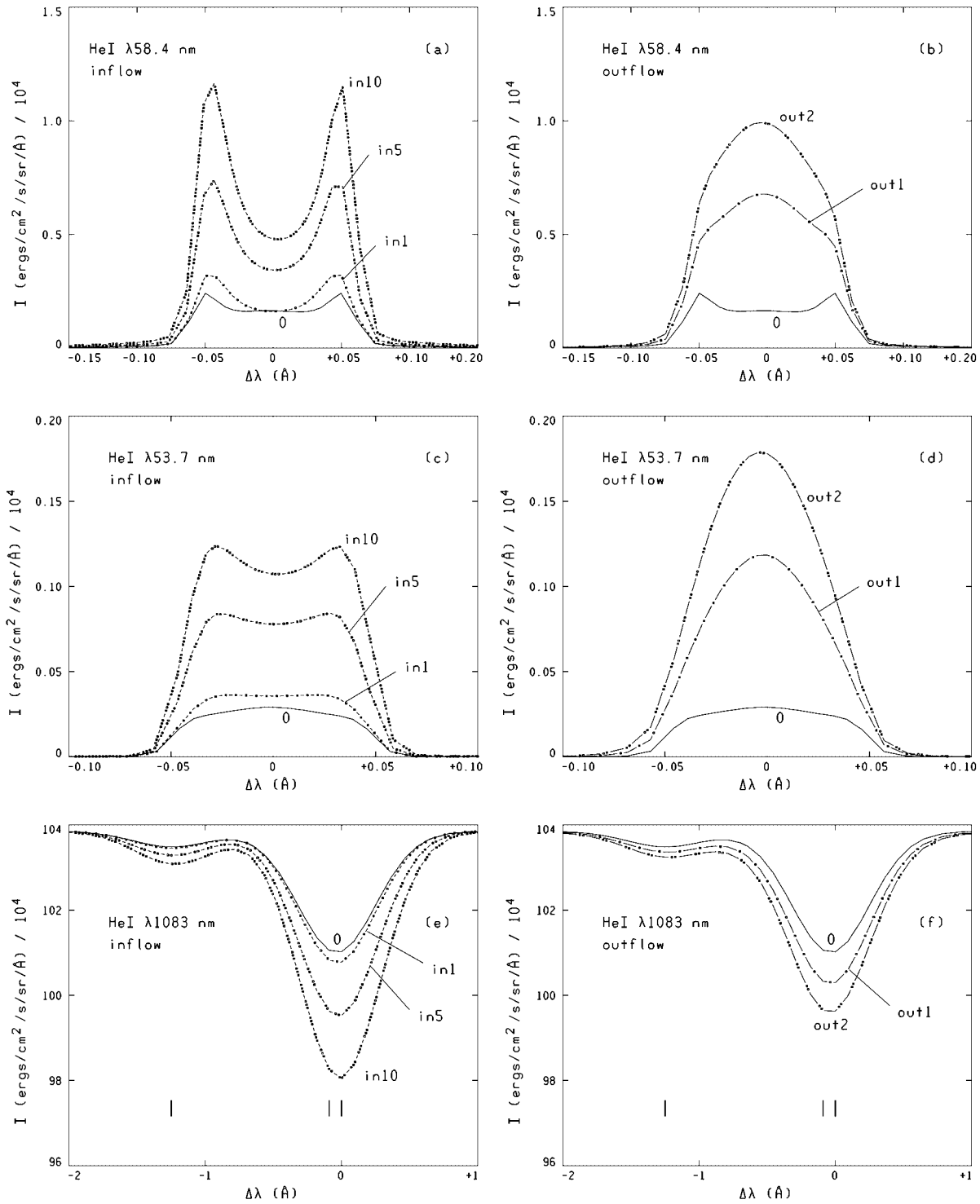

FIG. 12.—Calculated disk center He I line profiles

of these bright lines would not be practical diagnostics of small flows. Rather, the magnitude of their self-reversal and their relative intensities would be better diagnostic tools.

6. DISCUSSION

The present paper improves on the work of previous authors in that we include the combined effects of particle diffusion and velocities in addition to full non-LTE radiative transfer in the calculation of the H and He ionization and in the calculation of consistent level populations and radiative losses. We confirm the results of CYP97, who found that downflows flatten the temperature gradient while upflows sharpen it, but most of our results differ from theirs quantitatively because the flow velocities affect the ionization and radiative losses of H and He. (Note that the H and He ionization strongly affects the reactive heat transport.) Furthermore, the effects of particle diffusion even make our static case differ from other static models (e.g., Kuin & Poland 1991), as explained in the FAL papers. The

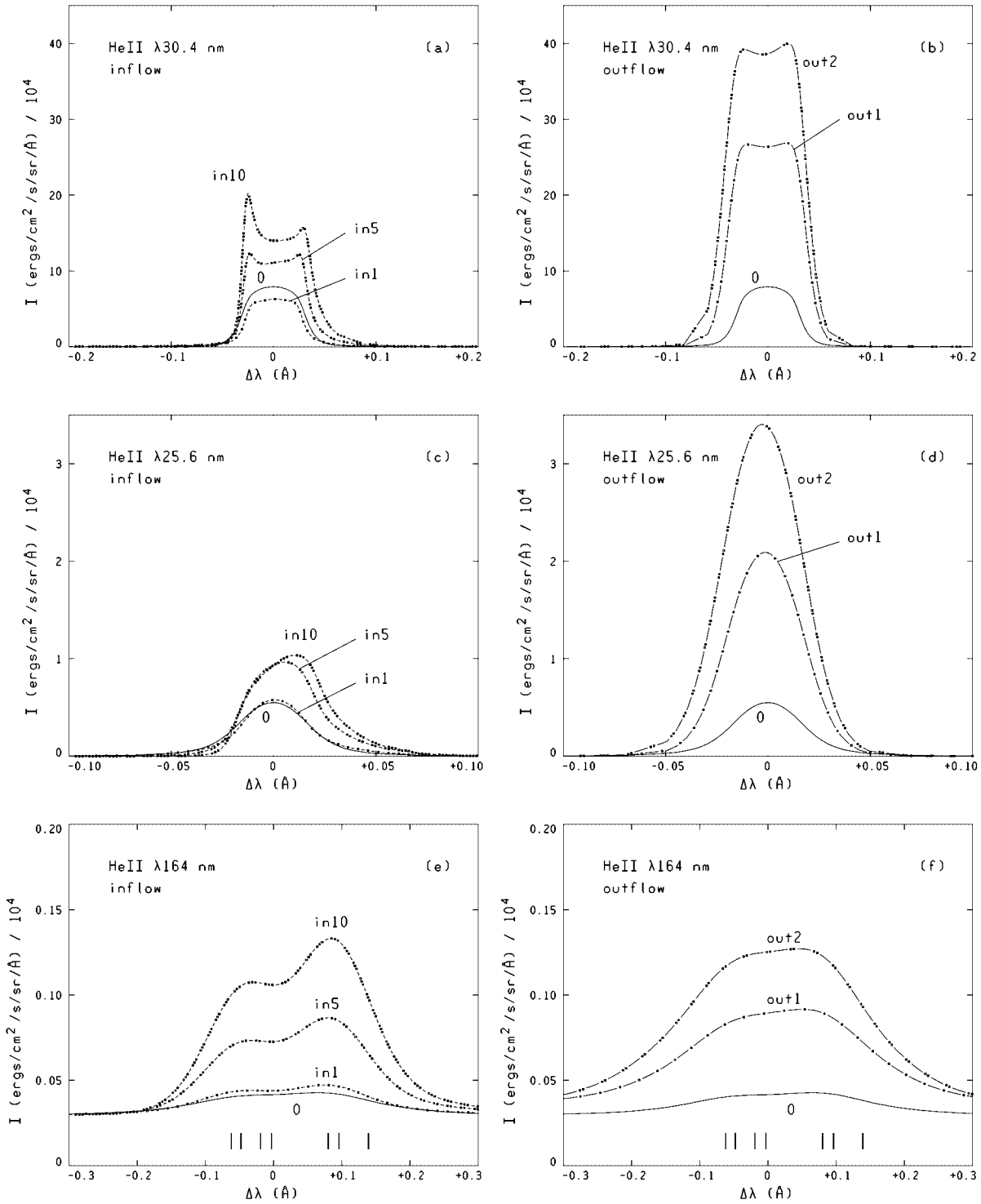

FIG. 13.—Calculated disk center He II line profiles

net result of all these differences is that in many cases our $T(z)$ distributions are shallower than those of CYP97 and that our values of the contributions to the heat flux differ from theirs.

In most of our models, the transition region has a small vertical extent. This region is located at the footpoints of loops that have a radius of several hundred kilometers. Consequently, the vertical radiative transfer is dominant except very close to the loop footpoint boundaries (as explained in FAL93). This would not strictly apply for models with large downflows, but still it may be a satisfactory approximation. In Tables 2 and 3 we have shown the values $z - z_0$ for 2×10^4 and 10^5 K, respectively. In the extreme case of model in10 the extent of the transition region from z_0 up to $T = 2 \times 10^4$ K is about 30 km, so the vertical radiative transfer would dominate the core regions of loop footpoints of more than 300 km in radius. This is because of the combined effects of much larger horizontal optical depth and much smaller solid angle subtended by the sides of the footpoint structures. For that same model in10, the vertical

extent of the lower transition region (from z_0 up to $T = 10^5$ K) is about 100 km; thus, we can say that the horizontal radiative transfer can be neglected in the core of a loop footpoint when the radius is more than 1000 km. Many loop radii in the lower transition region are probably between 300 and 1000 km, although observations have not yet provided accurate values. Thus, horizontal radiative transfer may somewhat affect the fast inflow cases, but it is hard to tell in which way because a complete three-dimensional radiative transfer calculation is needed. In addition, the three-dimensional calculation should include a number of complicated effects, such as flux tube expansion with height, inclination, and curvature. Such calculations would have to consider the nature of the surrounding environment, since that environment irradiates and is irradiated by the computed region. If the computed region were embedded in the corona, above the surrounding transition region, the conditions from the radiative transfer point of view would be similar to a dynamic prominence. (All these considerations apply only to the optically thick transitions. For the optically thin ones the three-dimensional effects would not be significant.) The orientation of the magnetic field with respect to the temperature and ionization gradients greatly affects the particle diffusion and momentum balance, and our current models assume that all these vectors are aligned. Such three-dimensional effects are very complex and beyond the scope of this paper.

The boundary parameters at the base of the transition region in our calculation characterize the top of the chromosphere and are density, temperature, H and He ionization, He abundance, temperature gradient, H and He ionization gradients, H and He particle flows, and turbulent pressure. (Magnetic topology can be added when a magnetic field structure more complicated than a vertical magnetic field is considered.) In principle, we could instead choose to specify these parameters at the coronal boundary. While boundary conditions can be prescribed in many ways, it is often easier to compute models by fixing them at just one of the boundaries. The results obtained in this way, then, define the values of the parameters at the other boundary. Thus, one can adjust the prescribed chromospheric boundary conditions to match coronal observations as well. Again, we note that since the chromospheric layers are affected by the combination of radiation arriving from the photosphere below, and from the transition region and even the corona above, specifying a fixed radiation field incident on the transition region is not realistic, as noted earlier. Instead, we solve simultaneously the radiative transfer and ionization and excitation for the complete interdependent system including photosphere, chromosphere, and transition region. Currently we do not compute the incident coronal radiation but use the values at wavelengths below 80 nm given by Tobiska (1991), as given in Table 6 of FAL93. This may only be a rough approximation because coronal radiation is highly variable, and observed outflows on open field lines usually show diminished coronal radiation. However, the local value of the incident coronal radiation may not vary as much because of the averaging due to its optically thin nature. Besides, consistent coronal modeling is beyond the scope of this paper and requires considering three-dimensional geometry and magnetic field effects.

We compute the energy balance only in the transition region, where we assume that radiative losses are balanced mainly by the total heat flux from the corona (including the ionization energy flow, also called reactive heat flow) and by the enthalpy flow (outward or inward, depending on the particle flow). Note that the radiative losses (expressed per unit volume, and per unit mass, or in any other of the usual forms; see Fig. 10) in the transition region are orders of magnitude larger than those in the underlying chromosphere or the overlying corona. Thus, if one assumes that the mechanical energy dissipation in the transition region is comparable to that above and below, one concludes that mechanical energy dissipation in most cases would have only minor effects in the transition region. In our calculation of the transition region we therefore set mechanical energy dissipation equal to zero (but this is just a simplifying approximation since some dissipation is likely).

However, it is essential to include mechanical dissipation when computing the temperature structures of the chromosphere and the corona (regions that indirectly affect the transition region as well). If mechanical energy dissipation (other than by the mass flow) were included in our calculations, even in the primitive form of equation (38), then the onset of the large temperature gradient would move to a greater height, and this gradient itself would change more slowly. Such energy dissipation would partially compensate for the enthalpy flow in the case of strong outflow. Thus, if we included energy dissipation, we should be able to obtain solutions for larger outflows than those considered in this paper. We plan to address this in the future.

Furthermore, we do not extend our current models high into the corona since without mechanical dissipation the radiative and conductive losses require the temperature to rise unchecked. Mechanical energy dissipation balances the radiative and conductive losses at coronal temperatures, allowing the calculation of loop models that reach a maximum temperature. In addition, if sufficient heating is provided to balance the radiative losses in the upper transition region, it would be possible to compute models of cool loops like those studied by Oluseyi et al. (1999). That paper and the others cited therein provide a good introduction to the extensive literature on energy balance in coronal loops; the present paper applies to regimes that occur only at the footpoints of such loops and neglects complicated three-dimensional and radiative transfer effects that may arise when the transition region becomes very extended as a result of inflows.

As an example of an observation showing a system of "cool" coronal loops, we mention the famous group of large loops observed at the limb in C IV by the UVSP instrument on board the *SMM* spacecraft. These loops are an example of large dynamic loops at the solar limb (and were the logo of several publications). They were studied by Fontenla et al. (1989). As that paper suggests, and as was later confirmed by X-ray observations from *SMM*, that loop system was formed by condensation of material previously ejected by a small C flare at one of the footpoints. However, by the time the observation was made, the heating processes had subsided and the loops were cooling down, most likely as a result of radiative losses caused by the large density and relatively low temperature (estimated at $T \sim 10^5$ K). However, as the loops cooled down the material started falling (at a velocity estimated at $\sim$10 km s^{-1}), and this flow carried enthalpy (and ionization energy) down with it. Such energy downflow contributed to the cooling at the top and to the heating of the legs and feet of the loops. Persistent low-level brightening was observed at the visible foot (the other was

hidden by the disk), and this may be explained by the downward energy transport. Since this loop system was seen for many minutes with little change, it is likely that quasi-steady conditions prevailed at the legs and footpoints while the density slowly decreased at the top. Our models would apply to the footpoints of loops like these, where the velocities vary on timescales of many minutes. Small-scale phenomena of this type are common on the solar surface even in the quiet Sun, and they may be related to the H Lyα spicules and macrospicules (since these may just be the extended legs of dynamic coronal loops).

An observational test of the results presented here would be to compare high spectral resolution profiles of various lines obtained simultaneously for the same high-resolution spatial element at a footpoint of a coronal loop and to verify how the features of the various lines relate to each other and to the results shown here. We note that a particular observation may not match any of the results shown here because it may correspond to different boundary conditions than those we chose from our static model C. However, the trend of changes in line profiles and intensities of a set of lines of H and He, which might correspond to different flow velocities, could be compared with the present calculations.

Determining $T(z)$ based on energy balance is simpler in the transition region than in the underlying upper chromosphere. Energy balance models of the upper chromosphere must consider MHD effects that are probably negligible in the transition region. There are also other complicating factors that make the chromospheric problem very difficult. One of these is the need for accurate estimates of the radiative losses in the optically thick regime; such loss estimates need to account for the effects of velocities and, in many cases, for the effects of time-dependent flows.

Another complication for the calculation of the chromospheric structure is that mechanical energy dissipation is expected to depend on height, temperature, density, velocity, ionization, and magnetic field. However, until the mechanism of this mechanical dissipation is identified, these dependencies are also unknown (and there are too many scenarios to explore). By using a parametric formula like equation (38), one can only obtain a rough ad hoc estimate of C_q that corresponds approximately to the radiative losses of the static model C at some heights in the chromosphere. However, using equation (38) to compute energy balance models of the chromosphere may be practically meaningless since a single constant cannot account for the strong dependence on atmospheric parameters that would characterize any likely physical mechanism of chromospheric heating.

A further complication for the determination of the chromospheric structure is the likelihood of elemental abundance variations, caused by gravitational settling or electric fields. Solar wind measurements provide indications of such variations: in solar and stellar winds the abundances of elements with high first ionization potential (FIP), including He, differ from photospheric values (Meyer 1996). Just where in the solar atmosphere these abundance variations occur is currently not known, but the chromosphere is a good candidate. The study by Hansteen et al. (1997), discussed earlier, included a consideration of the variation of the abundance of helium relative to hydrogen, starting in the chromosphere.

We believe that the problem of chromospheric heating must be addressed by proposing plausible physical mechanisms. For a given mechanism we would need to (1) determine the dependence of the heating on the physical parameters, (2) compute the chromospheric structure resulting from the balance between this heating and the radiative losses, and (3) compare the predicted spectral signatures with observations from the entire range of heights of the chromosphere.

Although such a self-consistent approach is not simple, we believe that current computing resources are sufficient to attempt it. As we have shown in our papers on particle diffusion and here by our modeling of velocities in the transition region, consistent modeling of physical processes is a very powerful tool. It can produce results that compare well with observations and that explain features that are difficult to understand from oversimplified arguments. As shown by the case of the formation of the Lyα profile, often the explanations are simple once the main process is understood.

7. CONCLUDING REMARKS

We have presented here a fully self-consistent treatment of the radiative transfer, statistical equilibrium, and energy and momentum balance for the solar transition region that includes steady state mass flows as well as particle diffusion. The detailed calculations are carried out for H and He, while other elements are not treated in a fully self-consistent manner. However, these other elements have only a minor influence in the lower transition region, at temperatures between 10^4 and 10^5 K. We will address the effect of these elements on the upper transition region in the future.

We have shown results for various inward (or downward) and outward (or upward) particle flows. The cases shown here are only illustrative, and because of the large number of possible boundary conditions, it is beyond the scope of the present paper to include a grid of models. Instead, we have presented results for several cases to show the effect of various processes and to show how the flow velocities affect the emitted spectral lines of H and He and correspondingly the radiative losses.

Our calculated line intensities and profiles are generally consistent with the available observations (except for some details as discussed above). However, detailed comparison with observations would require specific adjustment of the boundary conditions for the observed case. Given the limited spatial resolution of many available observations, we may also need to combine the calculated spectra from various components for comparison with observations. All this is beyond the scope of the present paper.

We now comment on some of the generic results from our calculations. The progressive intensity increase of the Lyα peaks and increase of the relative depth of the central reversal (due to the much smaller line-center increase) with increasing inflow can be used as a diagnostic for small inflows that do not produce appreciable line asymmetry. In addition, the filling up of the line center with little changes to the line peaks and consequent reduction of the relative line reversal can be used as diagnostics of small outflows. Flows also affect the peak positions of Lyβ and especially the He II 25.6 nm line in a way that could be detected; these line intensities change less as a result of flows than as a result of conditions in different spatial features. (Compare the present profiles with those in FAL93 calculated for various typical quiet and active regions.)

The intensity ratios between H and He lines may well be affected by He abundance variations, and departures from the results shown here can be used to estimate such abundance variations. However, as we have shown, small flow velocities can affect these ratios. Thus, an analysis of these line ratios must include more than just a few lines since both the flow effects and the He abundance variation effects must be disentangled.

We think that the key to understanding the physical mechanisms in the solar chromosphere, transition region, and low corona and how they relate to the formation of solar spectra is not in assessing only one particular observation, or only one mean profile, but rather in observing the complete range of such features that are present in the Sun. In this way one can evaluate not only the mean spectra but also the variation of the spectra with position and time for various solar features. Such studies, together with the theoretical modeling of physical processes (and especially MHD processes, which have not yet been simulated in coupling the upper chromosphere with the low corona), would provide essential understanding of chromospheric and coronal heating as well as the origin of the solar wind.

Such studies are badly needed for the chromosphere (especially the upper chromosphere), where it is essential to improve upon the rough, unphysical approximations used so far and instead to treat MHD processes with realistic computations of the ionization, excitation, and radiative losses. We hope that the computations and methods shown here are a step in that direction and will encourage more self-consistent calculations and comparisons with observations.

This research has been supported in part by NASA grant NAG 5-9851. We thank the referee, Art Poland, for many constructive comments.

APPENDIX A

FIVE-DIAGONAL SOLUTION OF THE SECOND-ORDER EQUATION

The equation to be solved for $y(z)$ is

$$\frac{d}{dz}\left(gy - f\frac{dy}{dz}\right) + ry = s\,, \tag{A1}$$

where f, g, r, and s are assumed to be given at the discrete values of $z_i, i = 1, 2, \ldots, N$. We write the derivatives of any function $y(z)$ at depth i as

$$y'_i = \frac{y_{i+1} - y_{i-1}}{z_{i+1} - z_{i-1}} \tag{A2}$$

and in this manner obtain

$$\begin{aligned}(gy - fy')'_i &= \frac{1}{d_i}\left[(gy - fy')_{i+1} - (gy - fy')_{i-1}\right] \\ &= \frac{1}{d_i}\left\{\left[g_{i+1}y_{i+1} - \frac{f_{i+1}(y_{i+2} - y_i)}{d_{i+1}}\right] - \left[g_{i-1}y_{i-1} - \frac{f_{i-1}(y_i - y_{i-2})}{d_{i-1}}\right]\right\}\,,\end{aligned} \tag{A3}$$

where $d_j = z_{j+1} - z_{j-1}$.

Equation (A1) then becomes

$$E_i y_{i-2} + D_i y_{i-1} + C_i y_i + B_i y_{i+1} + A_i y_{i+2} = s_i, \tag{A4}$$

where

$$\begin{aligned}E_i &= \frac{-(f_{i-1}/d_{i-1})}{d_i}\,, \\ D_i &= \frac{-g_{i-1}}{d_i}\,, \\ C_i &= r_i + \frac{f_{i-1}/d_{i-1} + f_{i+1}/d_{i+1}}{d_i}\,, \\ B_i &= \frac{g_{i+1}}{d_i}\,, \\ A_i &= \frac{-(f_{i+1}/d_{i+1})}{d_i}\,,\end{aligned} \tag{A5}$$

for $i = 3, 4, \ldots, N - 1$.

For $i = 1$ and 2 we let

$$y'_1 = \frac{y_2 - y_1}{\Delta_1}\,, \tag{A6}$$

where $\Delta_1 = z_2 - z_1$, and for $i = N - 1$ and N we let

$$y'_N = \frac{y_N - y_{N-1}}{\Delta_N} , \tag{A7}$$

where $\Delta_N = z_N - Z_{N-1}$. As a result,

$$\begin{aligned}
E_1 &= D_1 = 0 , \\
C_1 &= r_1 - \frac{g_1 + f_1/\Delta_1 - f_2/d_2}{\Delta_1} , \\
B_1 &= \frac{g_2 + f_1/\Delta_1}{\Delta_1} , \\
A_1 &= \frac{-(f_2/d_2)}{\Delta_1} , \\
E_2 &= 0 , \\
D_2 &= \frac{-(g_1 + f_1/\Delta_1)}{d_2} , \\
C_2 &= r_2 + \frac{f_1/\Delta_1 + f_3/d_3}{d_2} , \\
B_2 &= \frac{g_3}{d_2} , \\
A_2 &= \frac{-(f_3/d_3)}{d_2} , \\
E_{N-1} &= \frac{-(f_{N-2}/d_{N-2})}{d_{N-1}} , \\
D_{N-1} &= \frac{-g_{N-2}}{d_{N-1}} , \\
C_{N-1} &= r_{N-1} + \frac{f_{N-2}/d_{N-2} + F_N/\Delta_N}{d_{N-1}} , \\
B_{N-1} &= \frac{g_N - f_N/\Delta_N}{d_{N-1}} , \\
A_{N-1} &= 0 \\
E_N &= \frac{-(f_{N-1}/d_{N-1})}{\Delta_N} , \\
D_N &= \frac{-(g_{N-1} - f_N/\Delta_N)}{\Delta_N} , \\
C_N &= r_N + \frac{g_N + f_{N-1}/d_{N-1} - f_N/\Delta_N}{\Delta_N} , \\
B_N &= A_N = 0 .
\end{aligned} \tag{A8}$$

The coefficients in equation (A4) then can be determined from the values of g, f, r, s, and z, and this five-diagonal set of equations can be solved for $y_i, i = 1, 2, \ldots, N$.

Note that our use of equation (A6) implies a choice of boundary conditions and leads to a complete specification of the coefficients. This is appropriate when the divergence of the particle flow and diffusion velocities are negligible. When there is substantial inflow or outflow, we assume that the first term in equation (A1) is zero at the upstream boundary, so that $y = s/r$ at this boundary. Thus, for inflow we let $C_1 = r_1$, $B_1 = 0$, and $A_1 = 0$, and for outflow we let $C_N = r_N$, $D_N = 0$, and $E_N = 0$.

APPENDIX B

HELIUM MASS FLOW WITH DIFFUSION

B1. He I

Equation (31) for He I is

$$\frac{d}{dz}\left(g_\alpha y_\alpha - f_\alpha \frac{dy_\alpha}{dz}\right) + r_\alpha y_\alpha = s_\alpha . \tag{B1}$$

From equation (17) of FAL93,

$$v_\alpha = v_{\rm He} + (y_\beta + y_\gamma) V_C + y_\gamma V_D \ , \tag{B2}$$

where

$$\begin{aligned} v_{\rm He} &= y_\alpha v_\alpha + y_\beta v_\beta + y_\gamma v_\gamma \ , \\ V_C &= \Delta_2 + d_{33} \frac{d}{dz} \ln \frac{y_\beta}{y_\alpha} + d_{34} \frac{d}{dz} \ln \frac{y_\gamma}{y_\beta} \ , \\ V_D &= \Delta_3 + d_{43} \frac{d}{dz} \ln \frac{y_\beta}{y_\alpha} + d_{44} \frac{d}{dz} \ln \frac{y_\gamma}{y_\beta} \ , \\ \Delta_2 &= d_{31} Z_x + d_{32} Z_a + d_{35} Z_T \ , \\ \Delta_3 &= d_{41} Z_x + d_{42} Z_a + d_{45} Z_T \ . \end{aligned} \tag{B3}$$

Expanding each $\ln(x/y)$ as $(\ln x - \ln y)$ and replacing $d\beta/dz$ by $(-d\alpha/dz - d\gamma/dz)$ leads to the result

$$\begin{aligned} V_C &= \Delta_4 - \left(\frac{d_{33} - d_{34}}{y_\beta} + \frac{d_{43}}{y_\alpha} \right) \frac{dy_\alpha}{dz} \ , \\ V_D &= \Delta_5 - \left(\frac{d_{43} - d_{44}}{y_\beta} + \frac{d_{43}}{y_\alpha} \right) \frac{dy_\alpha}{dz} \ , \\ \Delta_4 &= \Delta_2 - \left[d_{33} \frac{y_\gamma}{y_\beta} - d_{34} \left(1 + \frac{y_\gamma}{y_\beta} \right) \right] \frac{d}{dz} \ln y_\gamma \ , \\ \Delta_5 &= \Delta_3 - \left[d_{43} \frac{y_\gamma}{y_\beta} - d_{44} \left(1 + \frac{y_\gamma}{y_\beta} \right) \right] \frac{d}{dz} \ln y_\gamma \ . \end{aligned} \tag{B4}$$

Thus, in equation (B1) we have

$$g_\alpha = F_{\rm He} + n_{\rm He} [(y_\beta + y_\gamma) \Delta_4 + y_\gamma \Delta_5] \tag{B5}$$

and

$$f_\alpha = n_{\rm He} \left\{ \left(1 + \frac{y_\gamma}{y_\beta} \right) [d_{33}(1 - y_\gamma) - d_{34} y_\alpha] + \frac{y_\gamma}{y_\beta} [d_{43}(1 - y_\gamma) - d_{44} y_\alpha] \right\} \ . \tag{B6}$$

We then solve equation (B1) for y_α by the method described in Appendix A.

B2. He II

Equation (31) for He II is

$$\frac{d}{dz} \left(g_\beta y_\beta - f_\beta \frac{dy_\beta}{dz} \right) + r_\beta y_\beta = s_\beta \ . \tag{B7}$$

From equation (17) of FAL93,

$$v_\beta = v_{\rm He} - y_\alpha V_C + y_\gamma V_D \ . \tag{B8}$$

Expanding the logarithmic terms in equation (C3) as before, but now replacing dy_α/dz by $(-dy_\beta/dz - dy_\gamma/dz)$, leads to the result

$$\begin{aligned} V_C &= \Delta_6 + \frac{1}{y_\alpha y_\beta} [d_{33}(1 - y_\gamma) - d_{34} y_\alpha] \frac{dy_\beta}{dz} \ , \\ V_D &= \Delta_7 + \frac{1}{y_\alpha y_\beta} [d_{43}(1 - y_\gamma) - d_{44} y_\alpha] \frac{dy_\beta}{dz} \ , \\ \Delta_6 &= \Delta_2 + \left(d_{33} \frac{y_\gamma}{y_\alpha} + d_{34} \right) \frac{d}{dz} \ln y_\gamma \ , \\ \Delta_7 &= \Delta_3 + \left(d_{43} \frac{y_\gamma}{y_\alpha} + d_{44} \right) \frac{d}{dz} \ln y_\gamma \ . \end{aligned} \tag{B9}$$

Finally, in equation (B7) we have

$$g_\beta = F_{\rm He} + n_{\rm He} (y_\gamma \Delta_7 - y_\alpha \Delta_6) \tag{B10}$$

and

$$f_\beta = n_{\rm He}\left\{d_{33}(1-y_\gamma) - d_{34}y_\alpha - \frac{y_\gamma}{y_\alpha}[d_{43}(1-y_\gamma) - d_{44}y_\alpha]\right\}, \tag{B11}$$

and we solve equation (B7) for y_β in the same way as described in Appendix A. Note that g_β and f_β, as well as r_β and s_β, depend on the values of y_α obtained from the He I solution, which in turn depends on the He II solution, but to a lesser extent. Thus, we solve equation (31) for y_α and y_β iteratively, until consistent values are obtained.

APPENDIX C

SOLUTIONS FOR CASES OF NEGLIGIBLE PARTICLE DIFFUSION

In the cases of large inflows the temperature gradient (and thus the ionization gradient) is very small, and diffusion effects become negligible. In these cases it is possible to obtain a formal solution of the ionization equation (13) by neglecting the diffusion velocity v_{ik}. In this case equation (13) can be written as

$$F_k \frac{dy_{ik}}{d\zeta_{ik}} + y_{ik} = \sigma_{ik}\ , \tag{C1}$$

where we use the definitions of the constant F_k and the ionization stage fraction y_{ik} given earlier. We define σ_{ik} as the value that y_{ik} should have if the flow were zero, i.e.,

$$\sigma_{ik} = \frac{s_{ik}}{r_{ik}}\ , \tag{C2}$$

and we define ζ_{ik} so that

$$d\zeta_{ik} = r_{ik}\, dz\ . \tag{C3}$$

This transformation is always possible because r_{ik} is always larger than zero, and it corresponds to

$$\zeta_{ik}(z) = \int_{z_b}^{z} r_{ik}(z')dz'\ , \tag{C4}$$

where z_b is the height at one of the boundaries of the region where equation (13) is evaluated.

Equation (C1) can be simply integrated from the boundary condition. In the following we omit all indices for simplicity. The solution is physically well behaved when the boundary condition for the integration is chosen to be closest to the origin of the flow, i.e., when z_b is the innermost height for outflow or the outermost height for inflow. The analytic solution is

$$y(\zeta) = y(0)\exp^{-\zeta/F} + \frac{\int_0^\zeta \sigma(\zeta')\exp^{-(\zeta-\zeta')/F}\, d\zeta'}{F}\ . \tag{C5}$$

A reasonable value to impose at the boundary is to let $y(z_b) = y(\zeta = 0) = \sigma(\zeta = 0)$. Note that y approaches s as F approaches zero. This analytic solution is possible only when $v_{ik} \approx 0$ because in general v_{ik} cannot be specified a priori but has to be solved with the diffusion theory that specifies its dependence on the density gradients and therefore on y_{ik}.

REFERENCES

Avrett, E. H., Fontenla, J. M., & Loeser, R. 1994, in Infrared Solar Physics, ed. D. M. Rabin, J. T. Jefferies, & C. Lindsey (Dordrecht: Kluwer), 35
Avrett, E. H., & Loeser, R. 1992, in ASP Conf. Ser. 26, Cool Stars, Stellar Systems, and the Sun: Seventh Cambridge Workshop, ed. M. S. Giampapa & J. A. Bookbinder (San Francisco: ASP), 489
Boris, J. P., & Mariska, J. T. 1982, ApJ, 258, L49
Chae, J., Yun, H. S., & Poland, A. I. 1997, ApJ, 480, 817 (CYP97)
Cox, D. P., & Tucker, W. H. 1969, ApJ, 157, 1157
Craig, I. J. D., & McClymont, A., N. 1986, ApJ, 307, 367
Dupree, A. K., More, R. T., & Shapiro, P. R. 1979, ApJ, 229, L101
Fontenla, J. M., & Avrett, E. H. 1992, in Proc. First *SOHO* Workshop: Coronal Streamers, Coronal Loops, and Coronal and Solar Wind Composition, ed. C. Mattok (SP-346; Noordwijk: ESA), 335
Fontenla, J. M., Avrett, E. H., & Loeser, R. 1990, ApJ, 355, 700 (FAL90)
———. 1991, ApJ, 377, 712 (FAL91)
———. 1993, ApJ, 406, 319 (FAL93)
Fontenla, J. M., Filipowski, S., Tandberg-Hansen, E., & Reichmann, E. J. 1989, ApJ, 344, 1034
Fontenla, J. M., Reichmann, E. J., & Tandberg-Hansen, E. 1988, ApJ, 329, 464 (FRT88)
Fontenla, J. M., White, O. R., Fox, P. A., Avrett, E. H., & Kurucz, R. L. 1999, ApJ, 518, 480
Hansteen, V. H., & Leer, E. 1995, J. Geophys. Res., 100, 21577
Hansteen, V. H., Leer, E., & Holzer, T. E. 1997, ApJ, 482, 498
Jefferies, J. T. 1968, Spectral Line Formation (Waltham: Blaisdel)
Kohl, J. P. 1977, ApJ, 211, 958
Kuin, N. P. M., & Poland, A. I. 1991, ApJ, 370, 763
MacNeice, P., Fontenla, J., & Ljepojevic, N. N. 1991, ApJ, 369, 544
Mariska, J. T. 1988, ApJ, 334, 489
———. 1992, The Solar Transition Region (New York: Cambridge Univ. Press)
McClymont, A. N. 1989, ApJ, 347, L47
McClymont, A. N., & Craig, I. J. D. 1987, ApJ, 312, 402
Meyer, J.-P. 1996, in ASP Conf. Ser. 99, Cosmic Abundances: Proceedings of the 6th Annual October Astrophysics Conference, ed. S. S. Holt & G. Sonneborn (San Francisco: ASP), 127
Mihalas, D. 1978, Stellar Atmospheres (San Francisco: Freeman)
Oluseyi, H. M., Walker, A. B. C., II, Santiago, D. L., Hoover, R. B., & Barbee, T. W., Jr. 1999, ApJ, 527, 992
Romanik, C. J. 1988, ApJ, 330, 1022
Rosner, R., Tucker, W. H., & Vaiana, G. S. 1978, ApJ, 220, 643
Saint-Maurice, J.-P., & Schunk, R. W. 1977a, Planet. Space Sci., 25, 243
———. 1977b, Planet. Space Sci., 25, 907
Tobiska, W. K. 1991, J. Atmos. Terr. Phys., 53, 1005
Vernazza, J. E., Avrett, E. H., & Loeser, R. 1973, ApJ, 184, 605
———. 1981, ApJS, 45, 635 (VAL81)
Wahlstrom, C., & Carlsson, M. 1994, ApJ, 433, 417
Warren, H. P., Mariska, J. T., & Wilhelm, K. 1998, ApJS, 119, 105
Woods, D. T., & Holzer, T. E. 1991, ApJ, 375, 800